DOE-GI-0000471-19

Final Scientific / Technical Report

Award Number: DE-EE0000471

Recipient: Giner, Inc.

Project Title: Transport Studies and Modeling in PEM Fuel Cells

Project Period: November 1, 2009 to July 30, 2014

Principal Investigator:

Cortney Mittelsteadt, Ph.D.
Vice President of Technology
781-529-0529; cmittelsteadt@ginerinc.com

Working Partners:

Giner, Inc./Giner Electrochemical Systems, LLC
University of South Carolina
Virginia Polytechnic Institute and State University Tech-Etch, Inc.

Project Officer:

Gregory J. Kleen
303-275-4875; gregory.kleen@go.doe.gov

DISCLAIMER

EXECUTIVE SUMMARY

This project's aim was to develop fuel cell components (i.e. membranes, gas-diffusion media (GDM), bipolar plates and flow fields) that possess specific properties (i.e. water transport and conductivity). A computational fluid dynamics model was developed to elucidate the effect of certain parameters on these specific properties. Ultimately, the model will be used to determine sensitivity of fuel cell performance to component properties to determine limiting components and to guide research. We have successfully reached our objectives and achieved most of the milestones of this project.

We have designed and synthesized a variety of hydrocarbon block polymer membranes with lower equivalent weight, structure, chemistry, phase separation and process conditions. These membranes provide a broad selection with optimized water transport properties. We have also designed and constructed a variety of devices that are capable of accurately measuring the water transport properties (water uptake, water diffusivity and electro-osmatic drag) of these membranes. These transport properties are correlated to the membranes' structures derived from X-ray and microscopy techniques to determine the structure-property relationship. We successfully integrated hydrocarbon membrane MEAs with a current distribution board (CBD) to study the impact of hydrocarbon membrane on water transport in fuel cells.

We have designed and fabricated various GDM with varying substrate, diffusivity and micro-porous layers (MPL) and characterized their pore structure, tortuosity and hydrophobicity. We have derived a universal chart (MacMullin number as function of wet proofing and porosity) that can be used to characterize various GDM. The abovementioned GDMs have been evaluated in operating fuel cells; their performance is correlated to various pore structure, tortuosity and hydrophobicity of the GDM. Unfortunately, determining a universal relationship between the MacMullin number and these properties was not achieved.

We have simulated fuel cell performance, current distribution and water distribution at various values of the water uptake, membrane diffusivity, and electro-osmotic drag coefficient (EODC) and compared modeling results with segmented-cell data for both serpentine and parallel flow-fields. We have developed iterations of fuel cell flow fields to achieve specific water transport and thermal management targets. This work demonstrated the importance of membrane diffusivity on fuel cell performance, the necessity of a high membrane diffusion coefficient, and the desirability of a low EODC at low levels of relative humidity.

TABLE OF CONTENTS

LIST OF TABLES

LIST OF FIGURES

1.0 INTRODUCTION

1.1 Project Objective

The overall objective of this project was to develop a better understanding of transport phenomena in current H_2/Air polymer electrolyte membrane fuel cells. Water transport and its role in fuel cell performance is the main focus of this project. The project objectives were achieved by generating custom materials, i.e., membranes, catalyst layers, diffusion media and flow fields, and characterizing them *ex situ*, followed by operation in a fuel cell and modeling of the results. Specifically, the project tasks were:

1. synthesis of block copolymers and determination of polymer structure and water state
2. determination of bulk membrane properties
    a. water uptake and diffusivity
    b. gas permeability
    c. electro-osmotic drag
    d. conductivity
3. fabrication and characterization of gas-diffusion layers (GDL)
4. fuel cell flow field manufacturing
5. fuel cell testing
6. fuel cell system modeling

Dr. James McGrath's group at Virginia Polytechnic Institute and State University (VA Tech) developed various block copolymers, as well as using transmission electron microscopy (TEM) and differential scanning calorimetry (DSC) to determine polymer structure and the state of water in these structures and their effect on transport properties. Giner, Inc. (Giner) determined the bulk membrane properties of water uptake and diffusivity, gas permeability and electro-osmotic drag utilizing test stations and apparatus currently being developed. Giner also made and tested membrane electrode assemblies (MEAs) from these materials. AvCarb, formerly Ballard Material Products, Inc. developed gas-diffusion layers consistent with specifications imposed by the University of South Carolina (USC) and Giner. We used Fuel Cell Technologies, GM's open source hardware, as well as custom hardware fabricated by Tech-Etch Inc. The University of South Carolina performed fuel cell testing and system modeling using computation fluid dynamics (CFD) packages.

1.2 Background

Fuel cell performance is greatly influenced by thermal and water management. Operation at high temperatures (i.e. >60°C) enhances electrode kinetics. However, high-temperature operation can yield to accelerated chemical and mechanical failures. It is well understood that Nafion®[1] membranes must be hydrated to conduct protons. Therefore, most fuel cell systems are operated with some level of humidification in the reactant gas. If the reactant humidity level is too low, the membrane water content could decrease sufficiently to render the membrane nonconductive; this would lead to low fuel cell operating potentials. Conversely, a very high level of humidification (or improper water management at the cathode, where water is produced) could

[1] Nafion is a registered trademark of E. I. du Pont de Nemours and Company

lead to flooding, in which the porous catalyst sites are effectively blocked from the reactants. Flooding also results in low fuel cell operating potentials. Thus, thermal and water management are key to achieving acceptable fuel cell performance.

These issues can be mitigated by properly designed fuel cell components. Thus, this project brings together groups with extensive experience in fuel cell membrane design and development (VA Tech), fuel cell membrane characterization (GES), GDL production (BMP), flow channel manufacturing (Tech-Etch) and system analysis and modeling (USC). The goal is to generate fuel cell components with specific transport-dependent characteristics (conductivity, porosity, hydrophobicity) to better understand their impact on water management and fuel cell performance. This should enable a fuel cell researcher to predict changes in performance based on fundamental properties of the fuel cell stack; more importantly, it should guide researchers to identify and develop those materials that limit stack performance most.

2.0 SUMMARY OF ACHIEVEMENTS

- Designed and synthesized a variety of hydrocarbon block polymer PEM membranes, 6FPAEB-BPSH, 6FPAEB-HQSH, 6FPAEB-SQSH (see their full names in Section 8), with lower equivalent weight, structure, chemistry, phase separation and process conditions. These membranes provide a broad selection of membranes with optimized water transport properties.
- Successfully casted the above copolymer powders to membranes and fabricated membrane electrode assemblies (MEAs) varying in size from 4″ x 4″ (for standard Fuel Cell Technology plates) to 12″ x 5″ (for GM plates).
- Designed, built and automated static and dynamic water uptake/diffusivity test system and completed water uptake and diffusivity measurements of the above hydrocarbon PEM membranes.
- Developed an open-ended hydrogen pump apparatus to characterize electro-osmotic drag coefficient (EODC) and measured it for Nafion membrane and the hydrocarbon PEM membranes.
- Designed segmented cell to quantify fuel cell voltage vs. current at different points along the active area. Segmented cells were used to identify regions of varying water transport and thermal management properties.
- Successfully integrated hydrocarbon membrane MEAs with current distribution board (CBD) to study the impact of hydrocarbon membrane on water transport in fuel cells
- Designed and made twelve gas-diffusion media (GDM) with varying substrate, diffusivity and micro-porous layer (MPL) and characterized their pore structure, tortuosity and hydrophobicity
- Evaluated the above GDM in operating fuel cells and correlated their performance to various pore structure, tortuosity and hydrophobicity of the GDM.
- Simulated cell performance and current distribution at various values of the water uptake, membrane diffusivity, and EODC and compared modeling results with segmented-cell data for both serpentine and parallel flow fields.
  Developed iterations of fuel cell flow fields to achieve specific water transport and thermal management targets.

3.0 RESULTS AND DISCUSSION

3.1 Membrane Structure and Properties

Two sets of hydrocarbon block copolymer membranes were designed and synthesized at VA Tech providing design guidelines for PEMs beyond Nafion membranes, as the structure, chemistry, and phase separation of copolymer blocks largely impact the transport properties in PEM fuel cells. Matrix 1 membranes (see **Table 1**) are based on block copolymer 6FPAEB-BPSH with various block length (7k-7k, 15k-15k, and 10k-18k), IEC (1.55 and 2.01 meq/g), annealing temperature (110 and 220°C). Matrix 2 membranes contain the same hydrophilic oligomer, BPSH, but a different hydrophobic oligomer, 6FK, 6FPAEB or 6FBPS0. Water uptake, conductivity, diffusivity, and EODC of these block copolymer membranes were characterized at Giner. The properties of these membranes were used by USC to simulate the fuel cell performance, water distribution, and current distribution, which were compared with experimental results of MEAs made from selected block copolymer membranes.

Table 1. Hydrocarbon Block Copolymer Matrix 1: Varied Block Length, IEC, Annealing Temperature

	Polymer	Thermal Treatment Temperature (°C)	IEC (meq/g)
1	6FPAEB-BPSH100 7k-7k	110	1.55
2	6FPAEB-BPSH100 15k-15k	110	1.55
3	6FPAEB-BPSH100 10k-18k	110	2.01
4	6FPAEB-BPSH100 7k-7k	220	1.55
5	6FPAEB-BPSH100 15k-15k	220	1.55
6	6FPAEB-BPSH100 10k-18k	220	2.01

Table 2. Hydrocarbon Block Copolymer Matrix 2: Varied Oligomer

6FPAEB-BPSH100	IV (dL/g)[a]	IEC(meq/g)[b]	Water Uptake(%)	Proton Conductivity[c] (S/cm)
Nafion 212	N/A	1.00	22	0.12
6FPAEB35 (random)	0.62	1.50	32	0.08
7k-7k	0.61	1.55	42	0.13
9k-9k	0.81	1.53	44	0.14
13k-13k	1.25	1.60	51	0.15
15k-15k	1.01	1.55	46	0.16
9k-13k	0.82	1.90	100	0.17
11k-15k	0.86	1.88	79	0.17
13k-17k	0.81	1.92	75	0.19

These membranes provide design guidelines for PEMs beyond Nafion membranes, as the structure, chemistry and phase separation of copolymer blocks largely impact the transport properties in PEM fuel cells.

The synthesis routes for 6FPAEB-BPSH are shown in **Figure 1**:

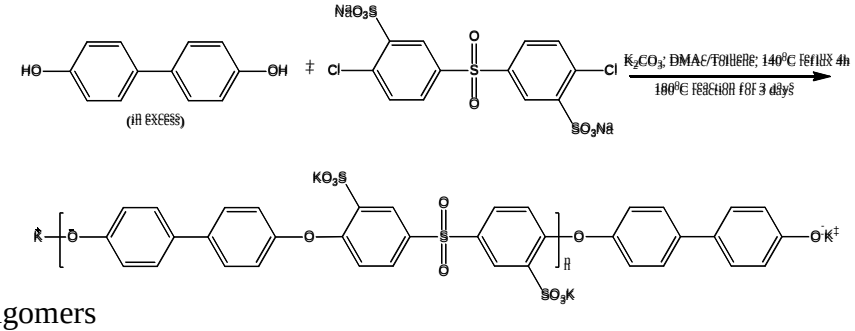

(a) BPS-100 oligomers

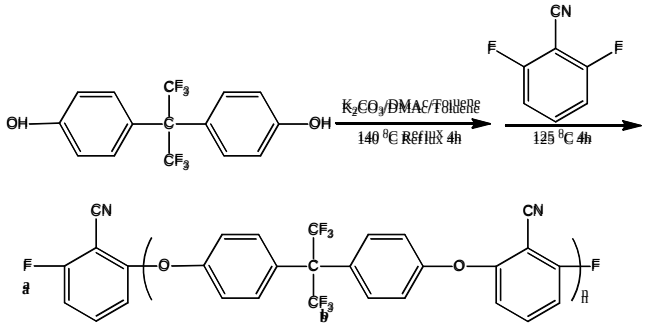

(b) 6FPAEB oligomers

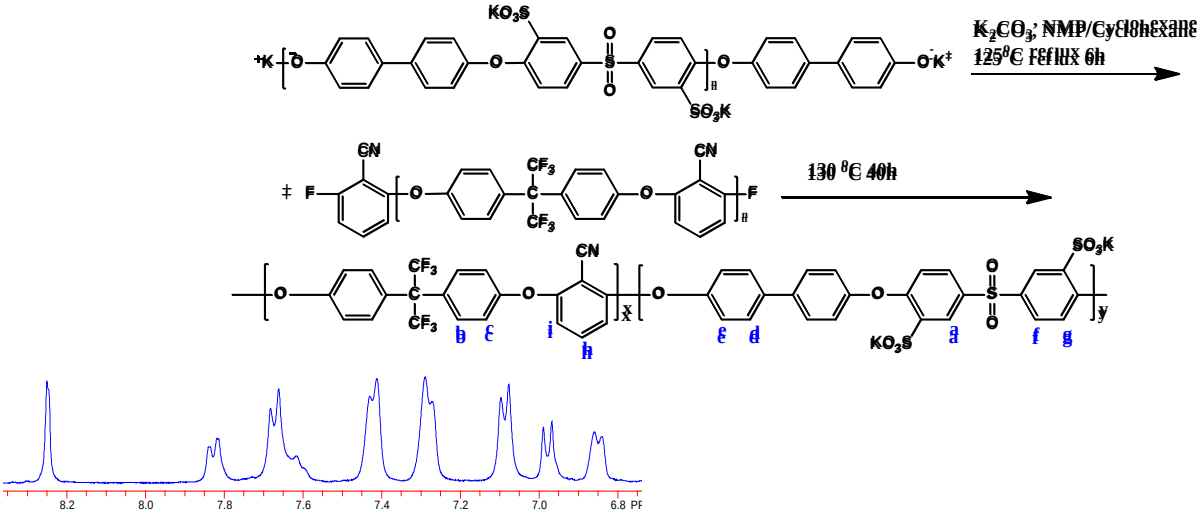

(c) BPS-100-6FPAEB copolymer

Figure 1. Synthetic routes for BPS-100 oligomers, 6FPAEB oligomers, and their copolymer

These membranes have been characterized by SAXS, TEM , TGA and a variety of techniques. **Figure 2** shows SAXS profiles of 6FPAEB-BPS100 multiblock copolymers, which confirm the presence of the ordered periodic microstructures and its dependence on the block length of the oligomers.

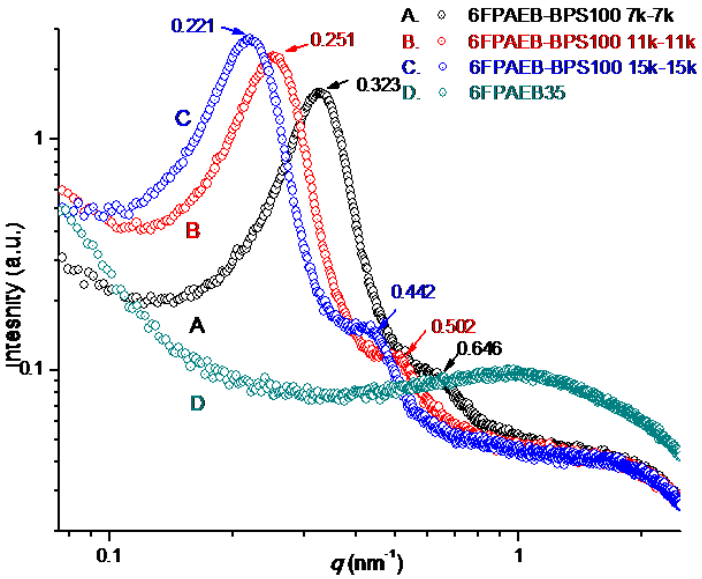

Figure 2. AXS profiles of 6FPAEB-BPS100 multiblock copolymers

Figure 3 shows TEM images of 6FPAEB-BPSH100 S copolymer. They clearly demonstrate nano-phase separated structures.

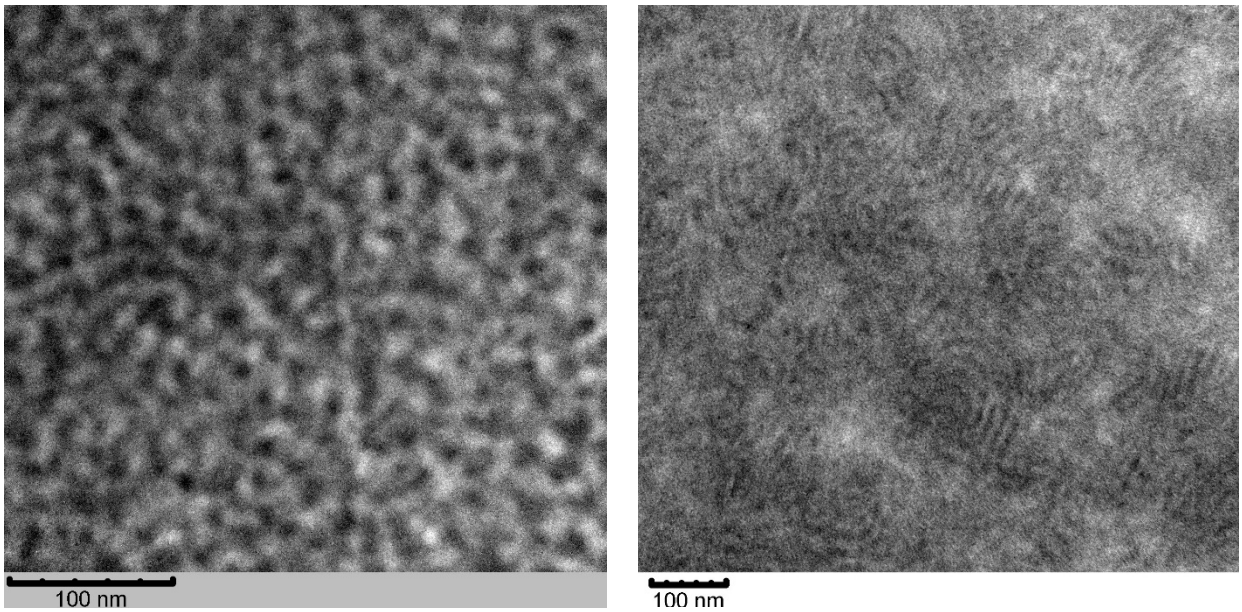

(a) 6FK-BPSH100 7k-7k (b) 6FK-BPSH100 15k-15k

Figure 3. TEM images of 6FPAEB-BPSH100 S copolymer

TGA thermograms were also performed, shown in **Figure 4**, which confirm good thermooxidative stability of 6FPAEB-BPSH100. The interaction between the nitrile groups and sulfonic acid groups on the main chains may induce the increased temperature of desulfonation and improve the thermooxidative stability of 6FPAEB-BPSH100 multiblock copolymers.

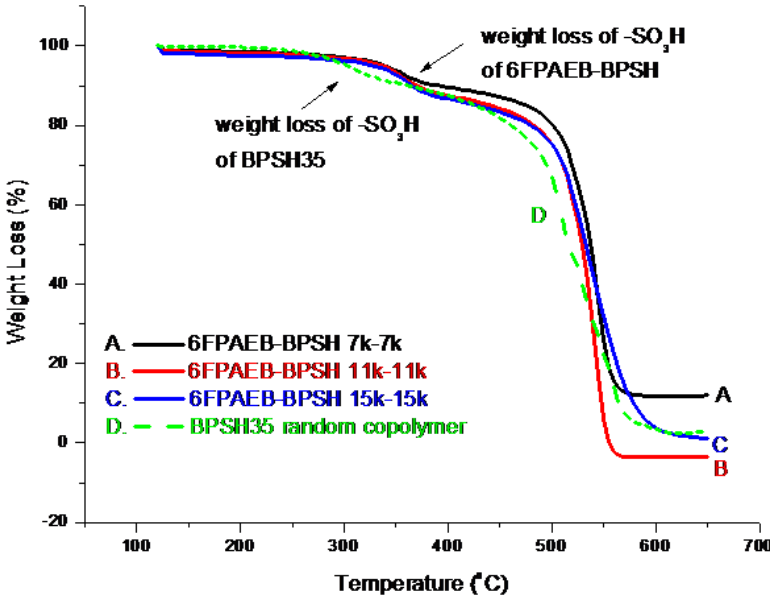

Figure 4. TGA thermograms of 6FPAEB-BPSH100

The synthesis of 6FPAEB-HQS100 is shown in **Figure 5**. The synthesis begins with HQS100 oligomer in DMSO/toluene that was treated with K_2CO_3 and reflux, and then coupled with 6FPAEB oligomer at 135°C for 48 hours.

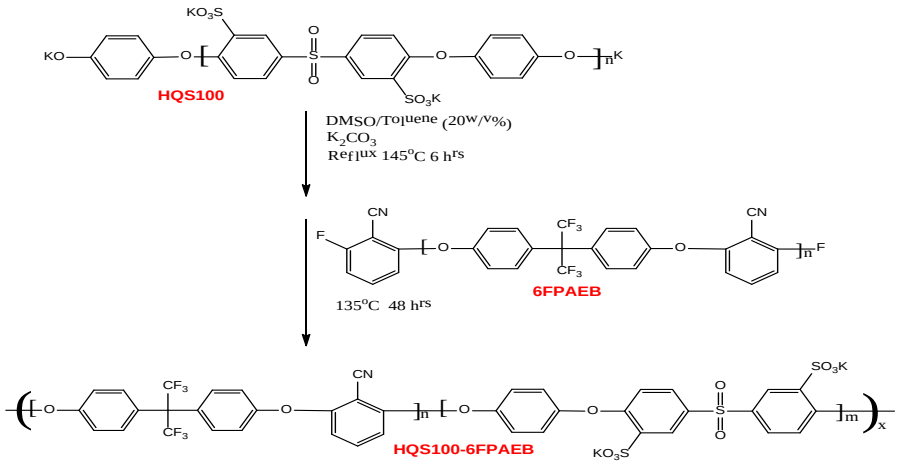

Figure 5. Synthetic route for 6FPAEB-HQS1000 coupling reactions

The water transport properties of 6K-6K 6FPAEB-HQS100 block copolymers are listed in **Table 3** in comparison with BPSH-6FPAEB copolymers and Nafion 212.

Table 3. Water Transport Properties of HQSH-6FPAEN

BPSH-6FPAEB	IEC (meq/g)a	Water uptake (%)	Proton Conductivity (S/cm)b
7K-7K	1.55	42	0.13
9K-9K	1.53	44	0.14
13K-13K	1.60	51	0.15
15K-15K	1.55	46	0.16
HQSH-6FPAEB			
6K-6K	1.76	49	0.15
9K-9K	1.65	55	0.15
11K-11K	1.50	64	0.15
Nafion 212	0.90	22	0.12

a. Measured using 1H NMR b: Measured in liquid water at 30^{o}C

Both BPSH-6FPAEB and HQSH-6FPAEB demonstrated higher charge density and water uptake and proton conductivity than Nafion 212 membranes. The proton conductivities of HQSH-6FPAEB multiblock copolymer at various RH were also measured in both forward (high RH → low RH) and backward direction (low RH to high RH). These results are compared against Nafion and biphenol-based block copolymers in **Figure 6**.

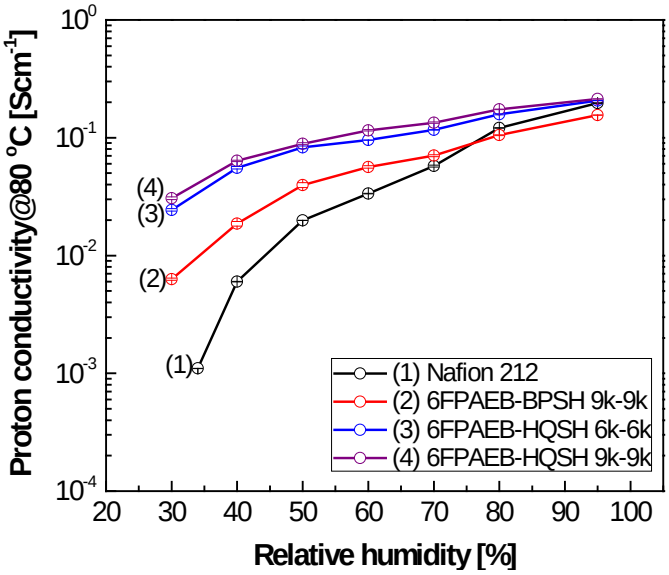

Figure 6. Conductivities of BPSH-6FPAEB block copolymers

3.2 Membrane Physical Properties

The focus in measuring membrane physical properties has been on measuring the diffusivity of membranes. Ionomers are well known to be highly permeable to water, and in fact are often used in saturator and dehumidification applications. The fact that transport occurs so quickly has made it difficult to measure, and many standard methods for measuring diffusivity fail. This occurs because diffusion of water though nitrogen and other gases to the membrane can often be much slower than diffusion through the membrane. Often times then, the rate of water transport through a membrane in a given RH gradient is not inversely proportional to membrane thickness. There is a disagreement in the literature as to whether this is due to diffusion outside of the membrane, or if an interfacial resistance exists with ionomers, which slows the equilibrium between water content in the vapor and membrane phase.

Giner has developed a novel approach to measuring the diffusion coefficient of water in fuel cell PEMs that eliminates all inert gases (and therefore diffusion *to* the membrane). This method consists of two sets of fuel cell hardware; one set of hardware serves as the membrane saturator and the other set is the diffusion cell. The membrane has liquid water on one side and water vapor on the other; the %RH of the water vapor side is controlled by a mini proportional valve. The diffusion cell has water vapor on both sides of the membrane, and the %RH difference is maintained at approximately 10% by the use of another mini proportional valve. A schematic of this system is shown in **Figure 7**.

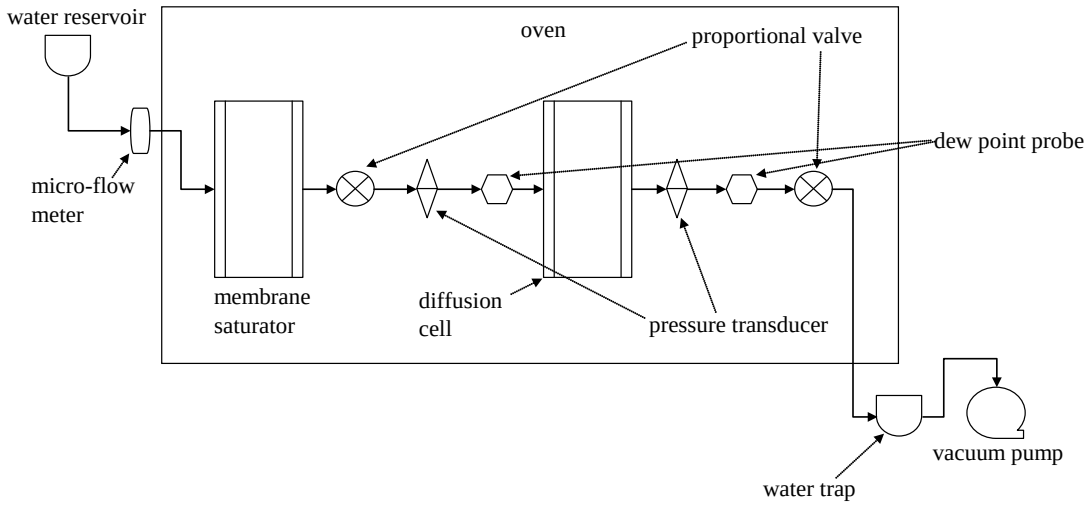

Figure 7. Schematic of diffusivity test station

Water transport through Nafion membranes of several thicknesses has been measured with the test station outlined in Figure 7; these results are shown in **Figure 8.** The water flux scales, within measurement error, with the membrane thickness. These results indicate that Fickian diffusion is the dominant resistance to the transport of water through the membranes, *and demonstrates the absence of an interfacial resistance*. These results are crucial in modeling water transport in fuel cell MEAs.

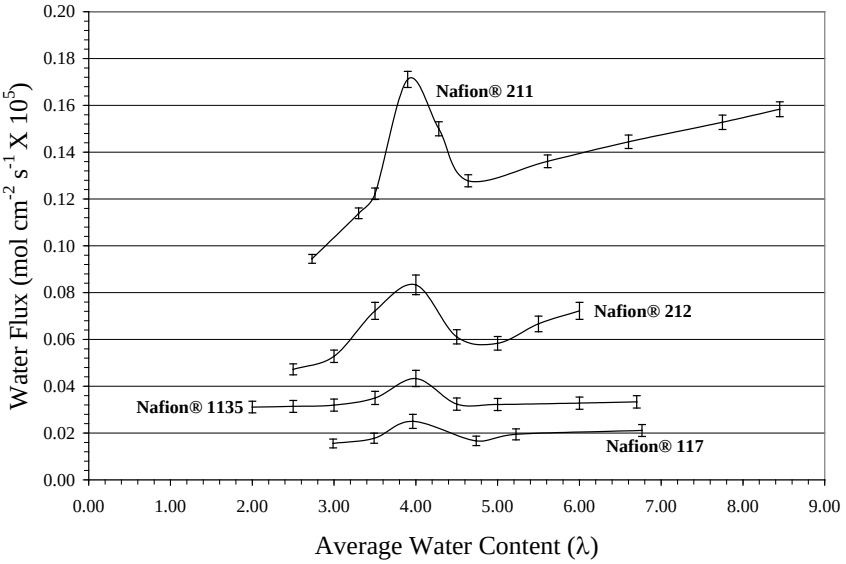

Figure 8. Water flux through Nafion membranes

The data shown in **Figure 9** allow for a better determination of the diffusion coefficient of water through fuel cell membranes. Several different values have been reported in the literature over the years; our results will help to standardize those values.

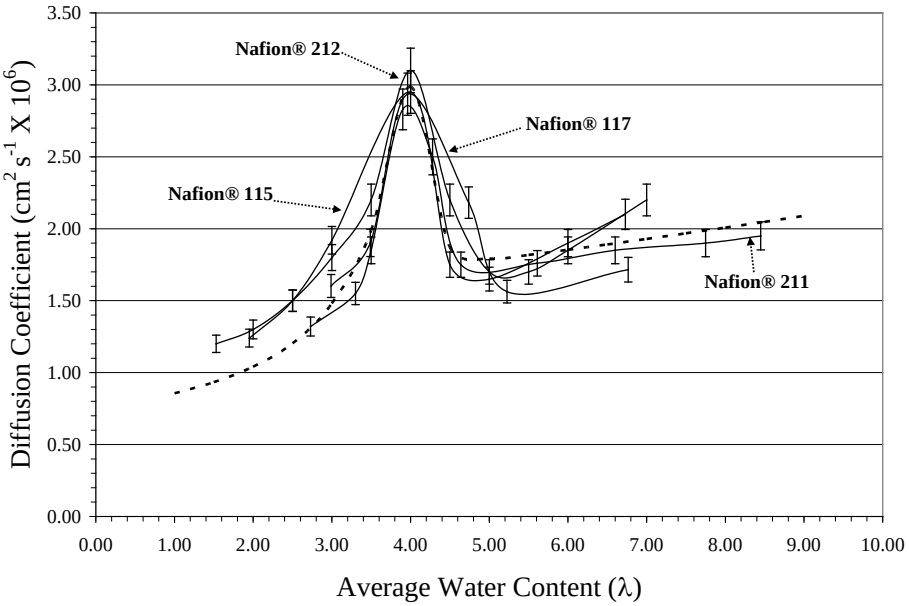

Figure 9. Water diffusion coefficient in Nafion membranes

The results shown in Figure 8 and Figure 9 were obtained at 80°C; measurement at other temperatures shows a similar trend, but the flux (and diffusion coefficient) is lower at lower temperatures, as expected. The dotted line in Figure 9 represents a model equation that has been fit to the data; this equation is a function of temperature, and thus can be used to predict the diffusion coefficient at different temperatures.

A second method of measuring diffusivity is also being developed. Similar to the first, it can reconcile different views of water transport, which is an essential step before developing a model. In the method outlined above, water moves across the membrane in a static gradient. The RH on either side of the membrane does not change, and therefore the membrane does not need to expand or contract with a change in water content. When RH conditions change, however, and water content changes, the membrane must make a physical change to accommodate that change in water volume. For example, when water content increases as RH increases, the membrane must expand against the physical matrix of the polymer chains. In this *dynamic* movement of water, the work needed to expand the membrane may slow diffusion and result in a different observed diffusivity. A method for measuring dynamic water uptake in fuel cell membranes has been developed, as shown in **Figure 10.**

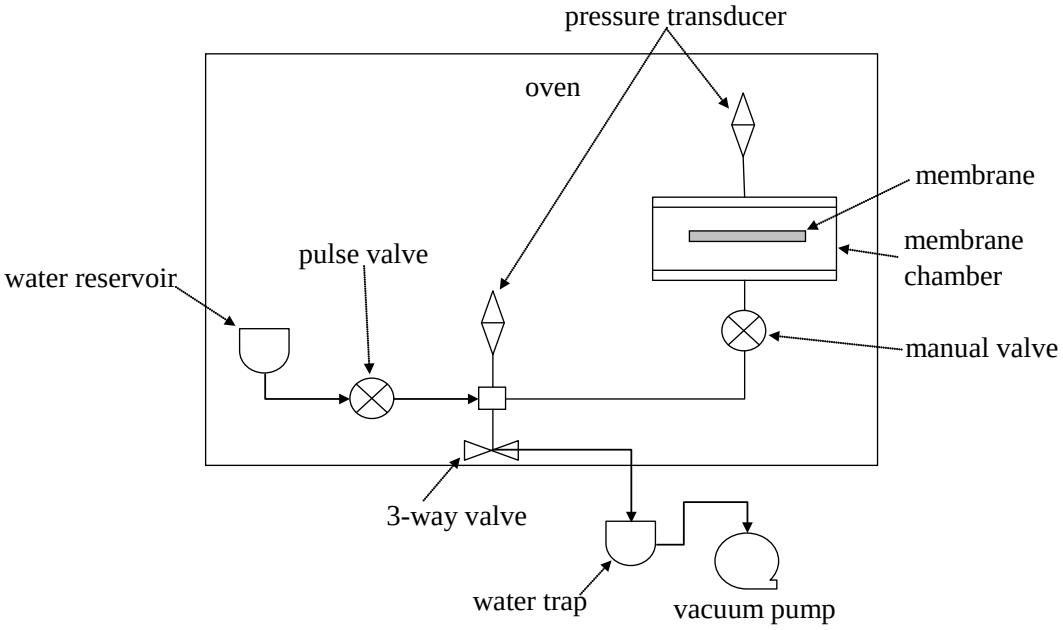

Figure 10. Dynamic water uptake test station

Dynamic water absorption for membranes is shown in **Figure 11**. First, the valve between the membrane chamber and the dead volume was opened; the system, including the chamber and the dead volume, was then vacuumed and later isolated from the vacuum pump; the valve between the chamber and the dead volume was closed to isolate these two units; a pulse valve placed between the water reservoir and the dead volume was opened allowing water vapor to enter the dead volume. Finally, the valve between the chamber and the dead volume was opened again, allowing the membrane to absorb water vapor present in the system. The data are also shown in Figure 11. It can be seen that absorption of water by the Nafion membrane is immediate, since there is no lag time between the equilibration of the two chambers and water absorption on the membrane. The instant diffusion of water into the Nafion membrane would indicate that the flux of water in the membrane is not a function of absorption kinetics.

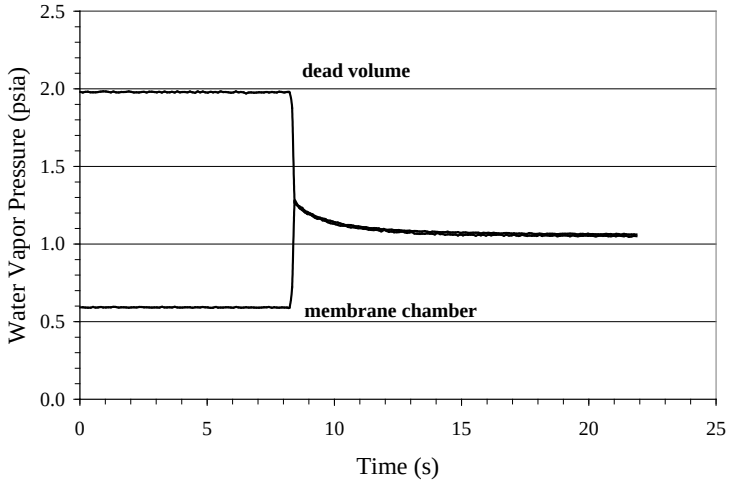

Figure 11. Dynamic water absorption curve for Nafion 212

The dynamic water uptake apparatus was modified to allow lower pressure and therefore lower temperature operation. The modification enables the system to reach vacuum as low as 0.01 psi, enabling water uptake and diffusivity of different membranes at low temperature to be characterized. The multiple-step membrane water absorption profiles at 30°C are compared with those at 80°C (see **Figure 12**).

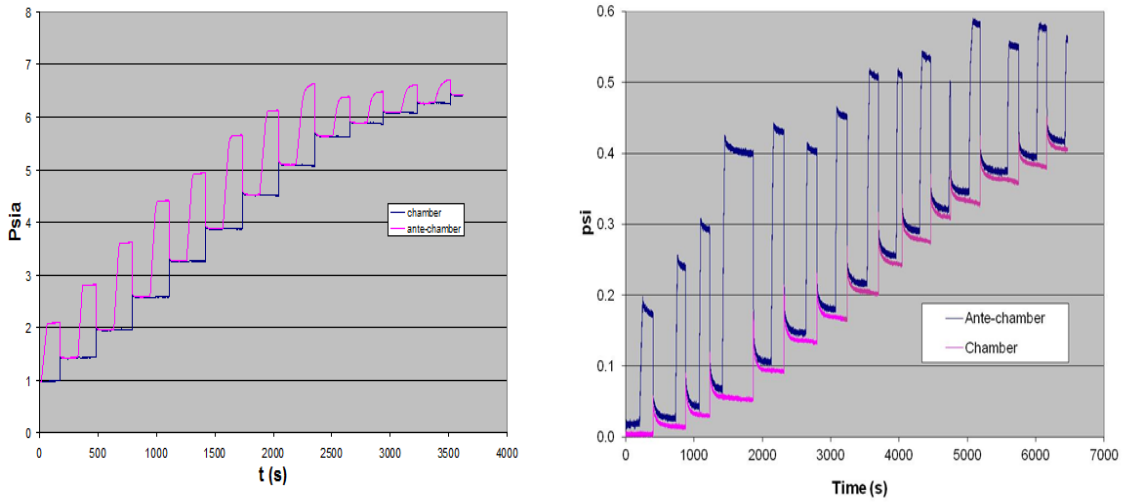

Figure 12. Membrane water absorption profiles at (a) 80°C and (b) 30°C

The above water absorption data (water vapor pressures at the chamber) were used to calculate the water uptake (Lambda λ, nH2O/SO3H), which is plotted against the relative humidity in **Figure 13**. At 80°C, Nafion 112 and BPSH-6FPAEB membranes exhibit similar water uptake profiles at RH lower than 70%. The subsequent divergence of water uptake could be due to the different membrane chemistry and structure of these membranes (function of polymer structure, cross-linking, thermal history). The temperature impact on the Nafion 112 membrane is negligible, while its impact on BPSH-6FPEAM appears more pronounced. The above water absorption data was also used to calculate water diffusivity using our well-established model.

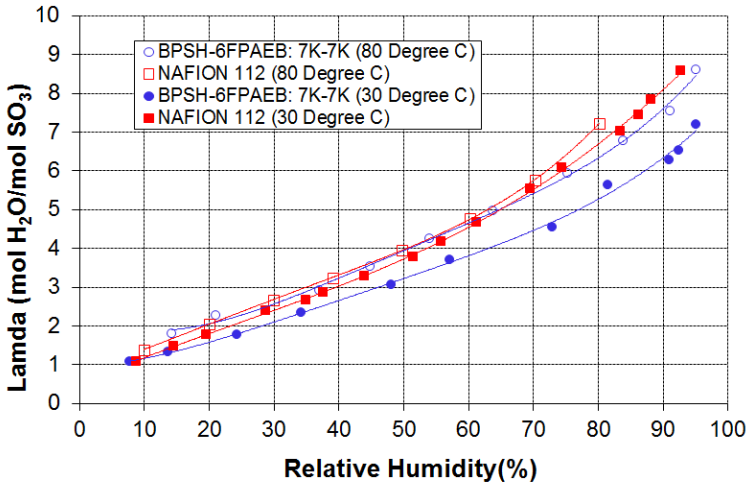

Figure 13. Comparison of membrane water uptake profiles at 80°C and 30°C

Water diffusivity of Nafion 112 and BPSH-6FPAEB at 30°C was plotted against relative humidity (See **Figure 14)**. The temperature impact on both membranes was apparent. For Nafion 112 membrane, water diffusivity at 30°C is 2-3 x 10^{-7} cm^2/s, which is almost one order of magnitude lower than that at 80°C. For BPSH-6FPAEB, water diffusivities at 30 °C are about 5-10 times lower than those at 80°C, dependent on the water uptake number.

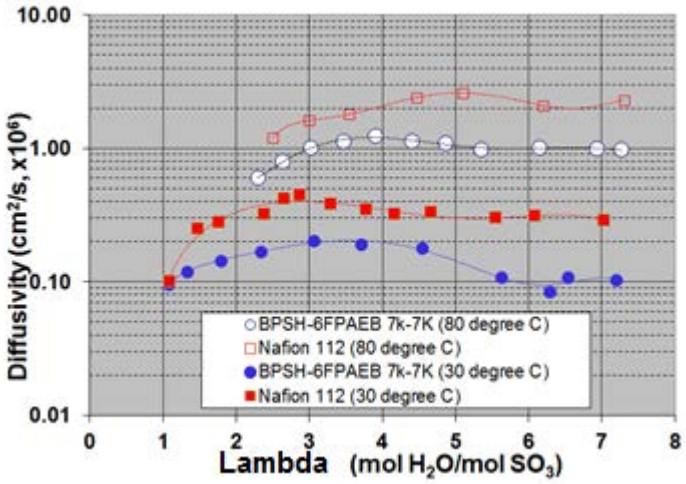

Figure 14. Comparison of membrane water diffusivity at 80°C and 30°C

The generation of the BPSH-6FPAEB with various chain length segments is documented in earlier reports. As expected, changing the chain length had little effect on the water uptake isotherms, as seen in **Figure 15**. Diffusivity is effected, however, with the smaller chain lengths having lower diffusivity than those with larger segments, as shown in **Figure 16**. The diffusivity of all of the hydrocarbon-based ionomers was significantly lower than that of Nafion. This was expected as the chain length increases, the scale of phase separation increases, and the water behaves more like "bulk water."

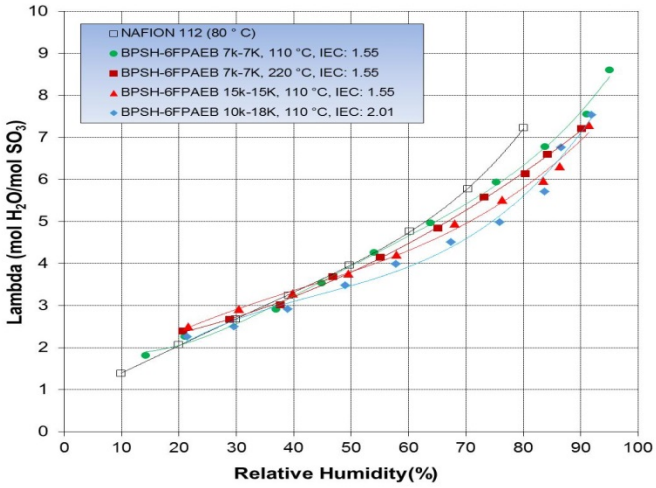

Figure 15. Isotherms of the BPSH-6FPAEB of various block lengths

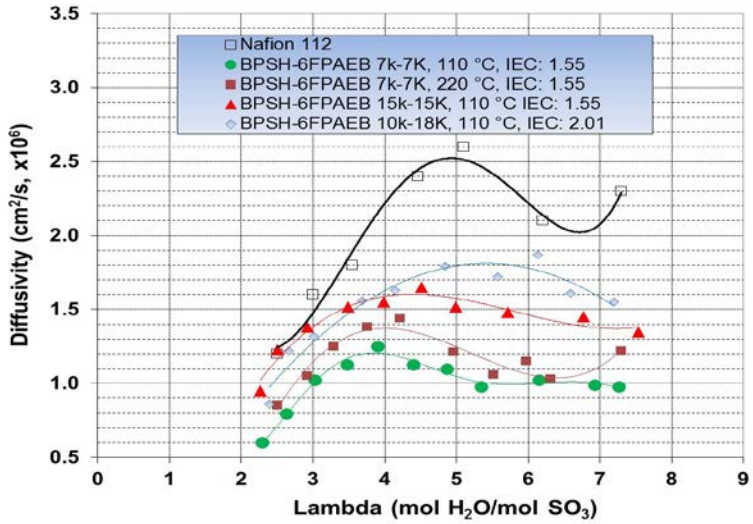

Figure 16. Diffusivity of the BPSH-6FPAEB of various block lengths

Giner developed a dead-end hydrogen pump-based system for EODC measurement. This system eliminated water vapor condensation and water diffusion. Both Nafion membranes and VA Tech membranes were characterized using this system. These results were compared with literature values.

The EODC characterization system consists of two cells: membrane saturator cell and hydrogen pump cell. Liquid water after a micro-flow meter feeds one side of the membrane saturator cell while hydrogen flows into the other side of the saturator cell that is pre-evacuated (see **Figure 17**). Water vapor pressure is controlled by the saturator oven temperature and total pressure is controlled by the hydrogen mass flow meter/pressure controller. By varying these two pressures we can control the water: hydrogen (H_2O:H) feed ratio. Protons generated by

hydrogen oxidation at the anode travel across the membrane and then are reduced to hydrogen at the cathode. The voltage of the hydrogen pump cell can be monitored; its stability depends on how close the feed ratio is to EODC. The ratio corresponding to the most stable voltage can approximate 2*EODC[1-2]. The most distinctive features of the system are that gas/gas diffusion is eliminated prior to the membrane surface, and there is a minimal RH difference between the inlet and outlet of hydrogen pump cell (<1%). Other advantages include precisely controlled water vapor (no condensation) and flexibility in RH and temperature variations.

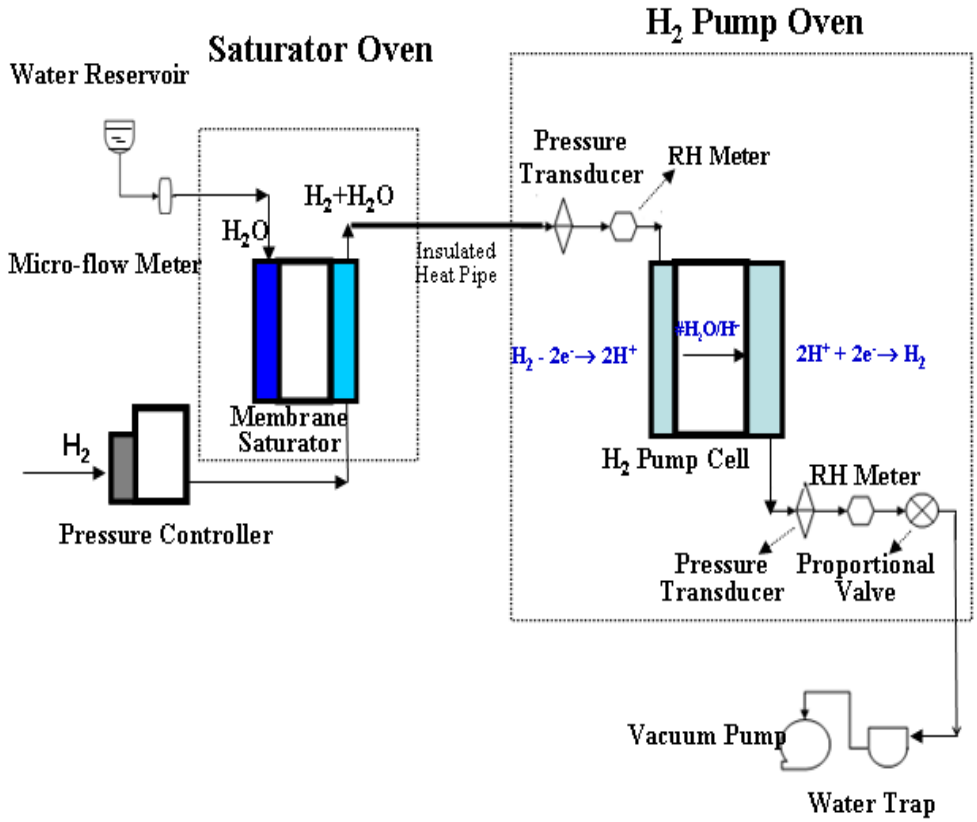

Figure 17. Dead-ended hydrogen pump EODC characterization system

If the feed ratio (H_2O:H) was less than the EODC, water molecules would be transported across the membrane more quickly than they were being fed to the anode, so the cell would dry out during the run as the water molecules on the anode that accompanied the protons across the membrane were not replaced. Cell voltage would increase, along with membrane resistance, until the experiment was stopped when the voltage rose above a set limit (generally 0.6 V). Likewise, if the feed ratio was greater than the EODC, water would accumulate on the surface of the anode and flood the electrode, at which point the voltage would rise rapidly (while membrane resistance would drop) until it surpassed the limit and the experiment was stopped. Only if the feed ratio was exactly equal to the EODC would the cell operate in a meta-stable steady state. Runs were conducted over a range of pressures until an optimally stable configuration was found and the EODC at the given temperature and humidity was determined.

The hydrogen pump cell was operated with a Nafion 115 membrane at 80°C, 82% RH at 100 mA/cm^2. When the feed ratio was initially as low as 0.21, the cell voltage increased rapidly due to the drying out of the membrane. As the feed ratio increased, the time for retaining stable cell voltage increased and reached the maximum when the F was 0.71. Afterwards, when the feed ratio further increased to 0.76, the time for cell voltage stabilization decreased due to flooding of the membrane (**Figure 18)**.

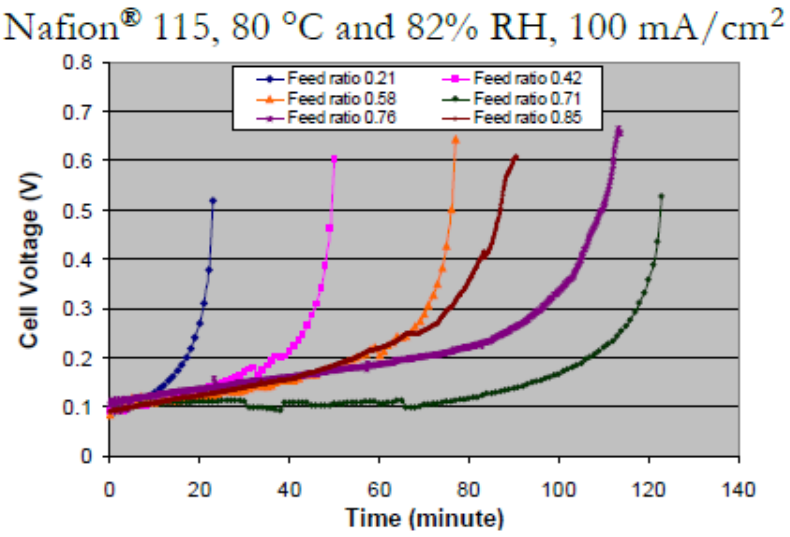

Figure 18. The change of cell voltage with time at various feed ratios

Multiple tests were performed using this methodology; the feed ratio with the longest stability time can be used to approximate the EODC (**Figure 19**).

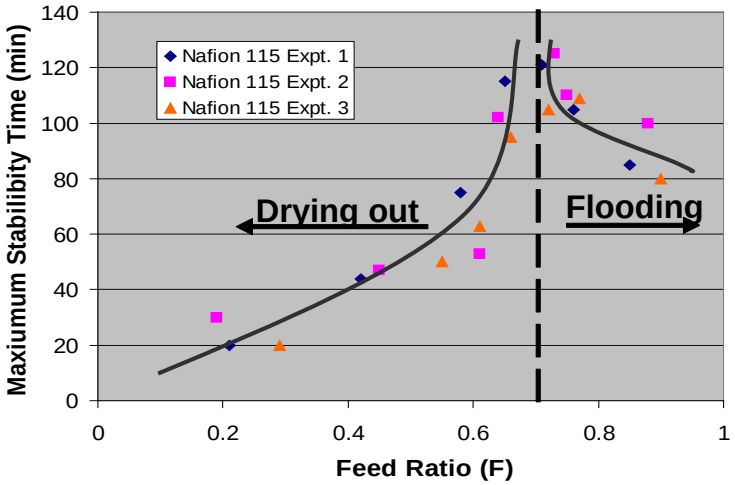

Figure 19. The change of maximum voltage stability time with feed ratio

The EODC of the hydrocarbon membranes with different chain lengths followed the same pattern as diffusivity. The polymers with shorter chain lengths showed lower EODCs over a wide breadth of water content, and all polymers were lower than Nafion (**Figure 20**). This is again attributed to the "tighter" water structure of the short-chain polymers. Under such confinement and demonstrated lower diffusivity, it is reasonable that the acid will be more tightly coordinated with the surrounding waters, favoring Grotthus hopping and thereby decreasing the EODC.

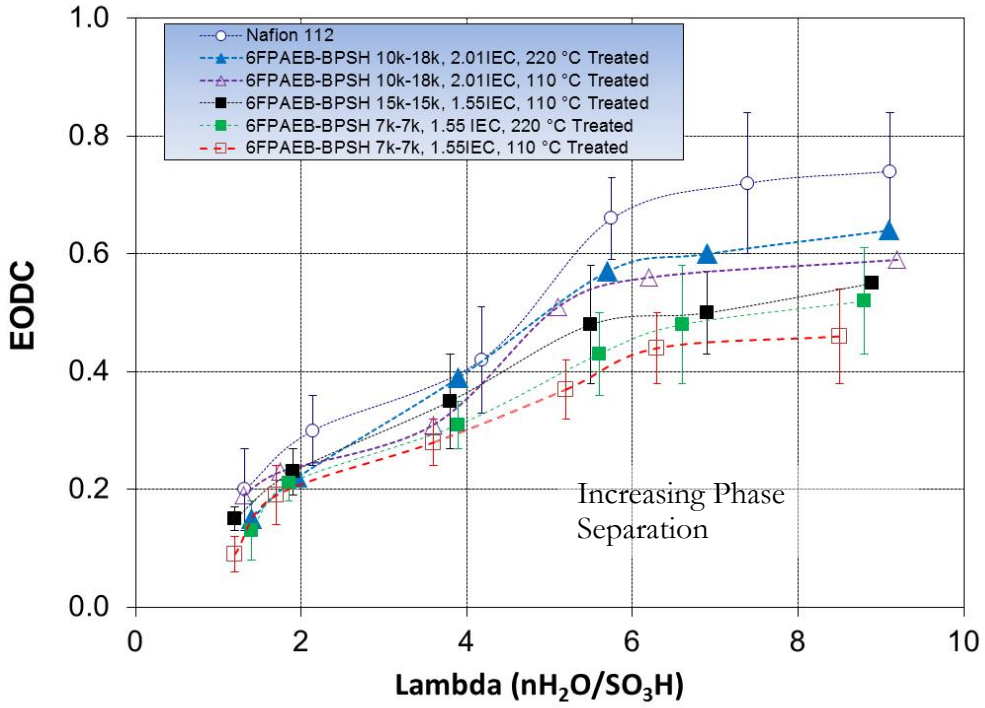

Figure 20. Electroosmotic drag coefficient of the BPSH-6FPAEB of various block lengths

3.3 Current Distribution Board (CBD) and Modelling

Kapton®[2]-based segment cells have been successfully designed to quantify fuel cell voltage vs. current at different points along the active area and tested the concept in common 50-cm^2 hardware first with only an addition of 1.5 mΩ resistance. The CBD was designed to have three main characteristics: non-invasiveness, low thermal insulation, and low cost. This CBD is placed inside a fuel cell during operation such that the cutout regions align with a triple-serpentine bipolar plate air channel to avoid obstruction of air during fuel cell operation. This alignment is illustrated in **Figure 21**. The CBD is capable of measuring 10 individual areas such that each area contains equal amount of conductor in the form of copper. Due to concerns with corrosion occurring after several uses, a gold flash was coated over the copper with a thin sub layer of nickel. The CBD consists of three layers: base, conductor, and a 2-mil Kapton board, which is

[2] Kapton® is a trademark of E. I. du Pont de Nemours and Company

used as the base layer. The conductor consisting of copper coated with gold is bonded to the Kapton by using Kapton adhesive. This adds about 2 mils of conducting material uniformly over the 10 individual current collection regions. Finally Kapton tape in the shape of a picture-frame insulates the conductor and maintains uniform thickness around the perimeter of the board to prevent leaks from occurring during operation.

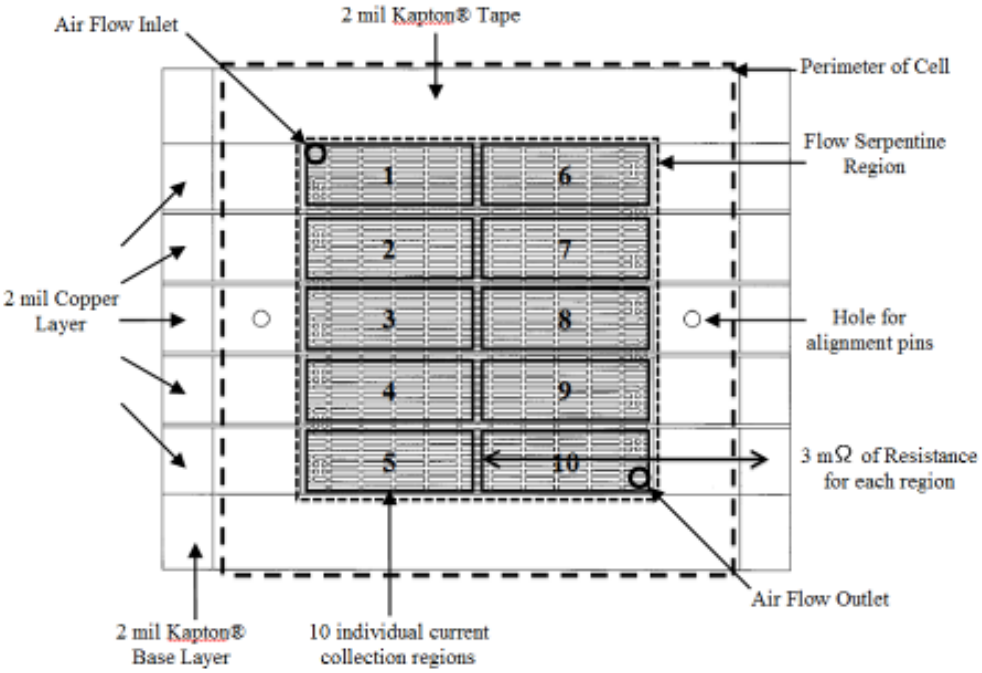

Figure 21. The current distribution board design

Custom CBD adaptors were machined to be lightweight and have excellent contact with the board and the current-carrying wire. Figure 21 illustrates the direction of current during operation and the contact points that the current will travel. The first contact point occurs between the CBD and a dual lug. Each lug allows two-point measurements for each of the 10 regions such that both current and voltage are measured and recorded. To prevent corrosion of these lugs, they also received a gold flash coating over their whole surface area. Using small screws to push the lugs against the board minimizes this contact resistance. The second contact point occurs between the lug and the current-carrying wire. This resistance is minimized due to the excellent contact maintained between the lug and the wire through the use of setscrews

During operation, the assembly of the fuel cell is demonstrated in **Figure 22**. When the cell is assembled, the CBD is placed with the conducting material facing the anode side, in the case of Figure 21, facing up towards the hydrogen side. Current is applied to the top end plate and flows through a GDL, MEA, 10 Individual H090 GDL pieces and finally ends at the CBD to exit the system to be measured by Hall Effect Sensors.

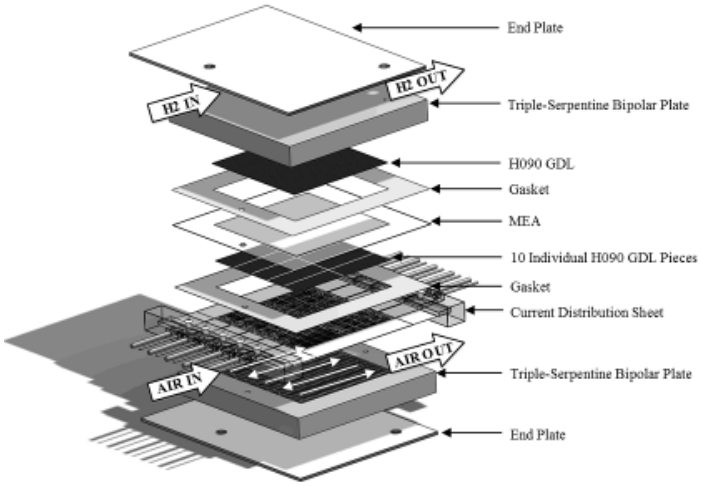

Figure 22. Assembly of fuel cell with current distribution board in place

To verify the setup and testing method, a mock test was used to collect the current distribution when using either a whole H090 GDL or an H090 GDL cut into 10 individual pieces. The purpose of the test was to observe if any current applied to one section would "smear" to another region due to the conductivity nature of the GDL. The current distribution was observed and recorded when running a fuel cell at various conditions. Note that the CBD is closest to the cathode (see Figure 22) while the conductive material faces the anode side of the cell. All the following tests were run at stoichiometries of 1.5 and 2.0 for the cathode and anode, respectively, at 80°C where the varying parameter was RH, which may affect water flooding more than any other parameter. **Figure 23** shows the distribution of the MEA current density for an RH of 25% on both the cathode and anode, at 80°C. The current density is greatest at the lower regions (outlet) which may be due to the overall higher water concentration relative to the higher regions (inlet).

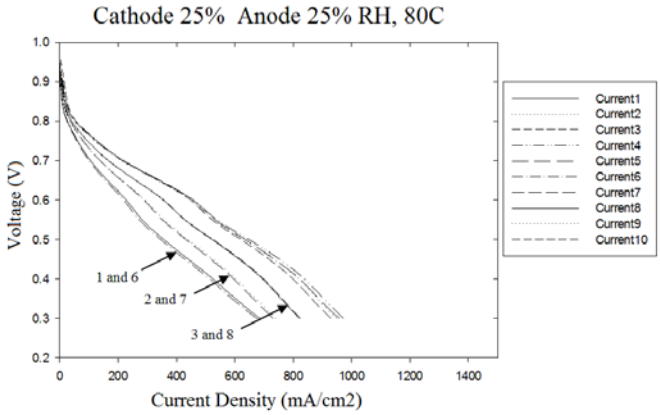

Figure 23. Current distribution for 80°C cell temperature, 25% RH at cathode and anode

Upon increasing the cathode relative humidity from 25% to 75% while maintaining the anode RH at 25%, the current density shows a different picture. From **Figure 24** the current density is now lowest at the lower regions of the cell (outlet). The lower regions (5 and 10) are indicated in the figure. However, the higher cathode RH does give improved current distribution throughout, except for lower voltage values.

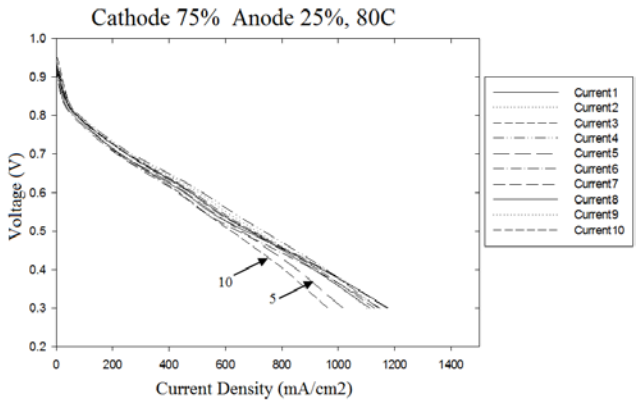

Figure 24. Current distribution for 80°C cell temperature, 75% RH at cathode and 25% RH at anode

USC completed experimental analysis of current density distributions on 50-cm^2 PEMFC with serpentine flow field under different inlet humidity. They also used CFD to model the current distribution and the results agree with the experimental analysis. **Figure 25** shows the performance comparison of the cells with and without a CBD at two anode RH conditions.

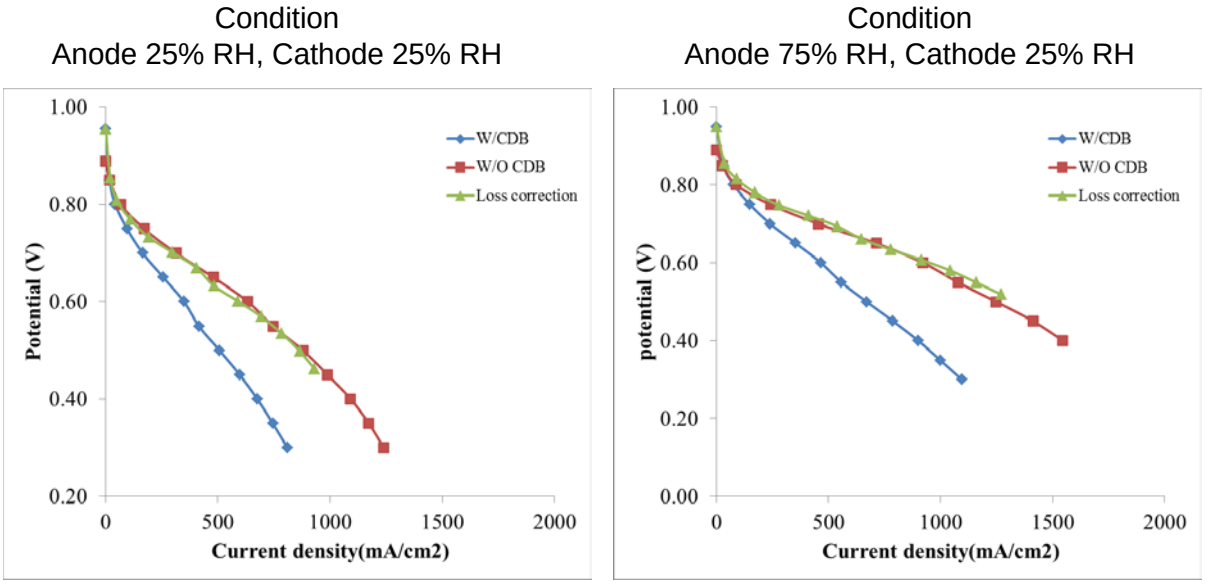

Figure 25. Performance comparison of the cells with and without a current distribution board

There is an apparent drop of the performance with the CDB. However, after correction was made based on 16% area loss & 4 mΩ from wires, the performance curve agrees well with that without the CDB. **Figure 26** shows current density distribution along flow field (inlet to outlet, up to down).

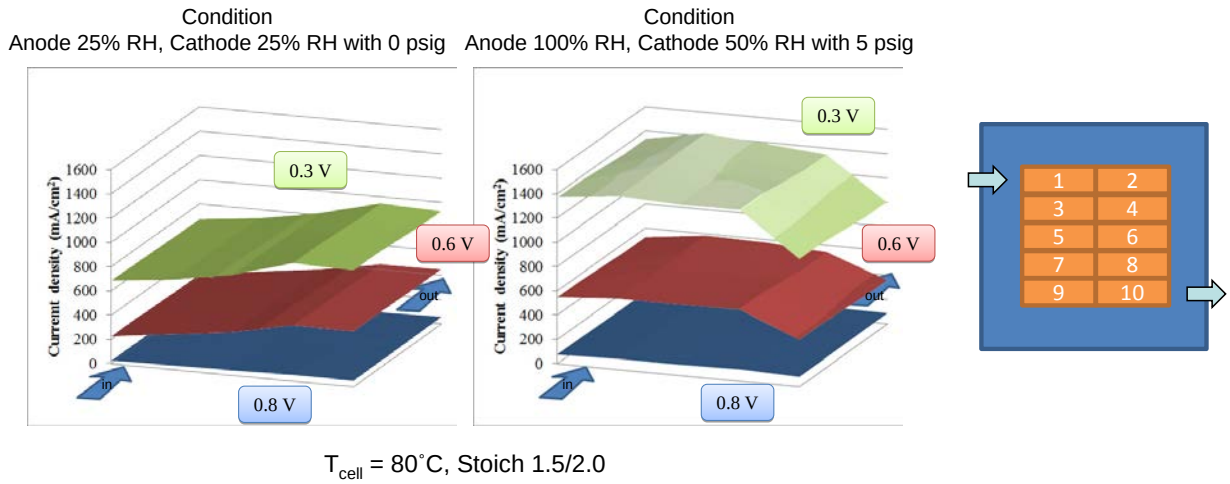

Figure 26. Current density distributions across flow field at three voltages

When the inlet is dry (25% RH anode and cathode), current distribution segments near the outlet display high current density because the actual RH near this region is high due to cumulative water from electrochemical reaction. At high inlet RH (100% RH anode and 50% cathode), current distribution segments near the inlet display high current density. This is because this region normally has high reactant concentration while the effect of produced water becomes negligible. CFD modeling was also performed to simulate current density distribution. These results are compared with experimental analysis in **Figure 27**. There are some discrepancies between CFD analyses and experimental results, but these discrepancies are within acceptable ranges provided that multiple assumptions were made in CFD simulations.

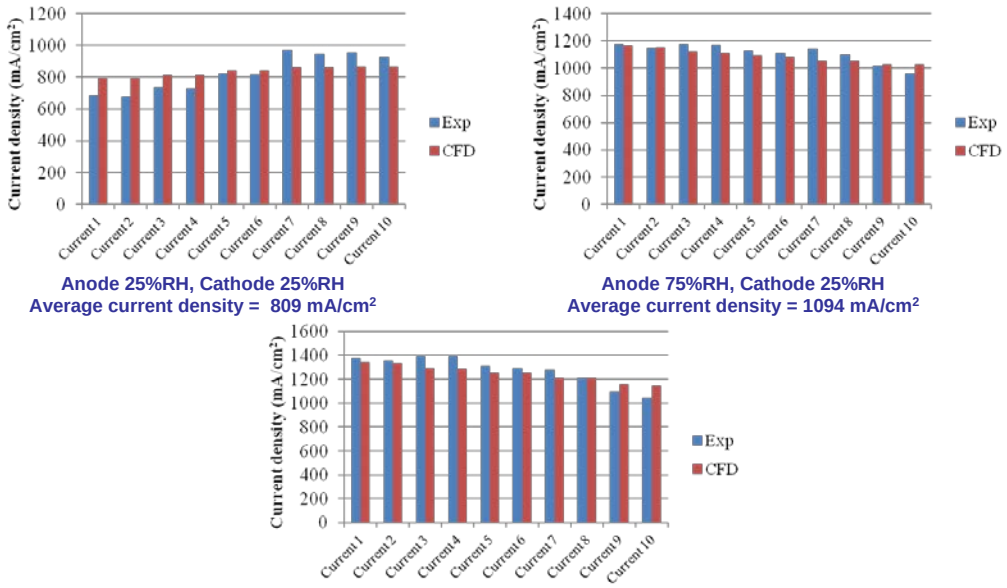

Figure 27. Experimental and CFD simulation of current density distribution (V = 0.3 V)

3.4 Gas-Diffusion Media (GDM) Manufacture and Modelling

This project designed 12 gas-diffusion media layers, GDM. The newly designed GDM were modified from standard Ballard GDM by adding two micro porous layers (MP1 and MP2). Each set has been treated with different methods to provide two different values of diffusivity. **Figure 28** illustrates the mercury pore size distributions of new design GDM. It can be seen that the baseline EP40T has the most pore volume compared to P75T and P50T. All three GDM have the maximum peak of differential distribution at pore diameter of 50 μm; modification of the GDM greatly reduces the volume of large pores.

The MacMullin number, which is a function of tortuosity and porosity, is often found to follow the equation below,

$$N_M = f(\tau, \varepsilon) = \frac{\tau^n}{\varepsilon^m}$$

This relationship has been previously used to characterize the GDM. The MacMullin number of these substrates does not appear to follow this relationship, as seen in Figure 28. The GDM with a micro porous layer (MPL) reduces the MacMullin number, which is consistent with the data from Toray TGP-H-060. Therefore, the N_M/ε profile of paper GDM with MPL moves more closely to the Bruggeman ($N_m \alpha \varepsilon^{-1.5}$) profile.

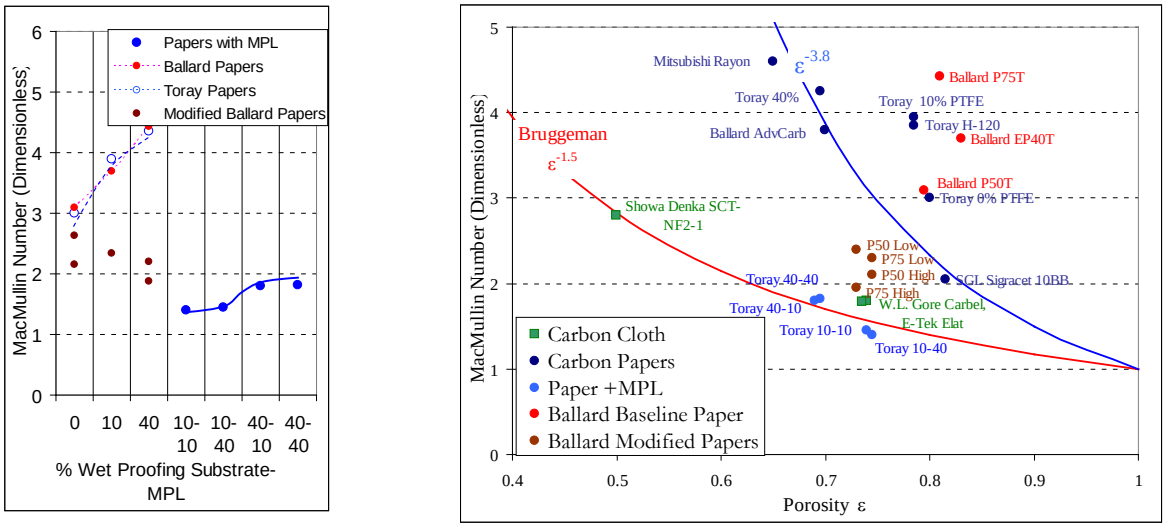

(a) **(b)**

Figure 28. MacMullin number as function of wet proofing (a) and porosity (b)

This project designed 12 GDM layers. Twelve custom GDM from AvCarb have been tested under selected humidity conditions. There are three different carbon substrates. They are EP40, P50, and P75. All of them have differences in thickness and properties (e.g., bulk density, permeability, porosity, tortuosity). After testing these substrates were modified by adding two micro porous layers (**Figure 29)**. Each of these was then treated with two different methods to provide two different values of diffusivity (i.e. <0.15 cm^2/s and >0.35 cm^2/s). Moreover, two micro porous layers have been constructed with two different sizes of carbon particle (i.e. small and large).

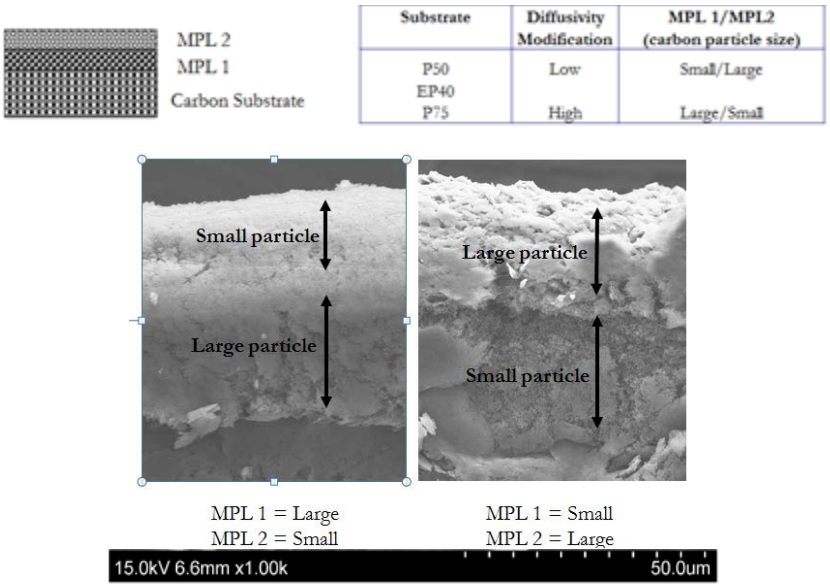

Figure 29. Design of custom gas-diffusion media from AvCarb and the SEM images of two micro layers

The pore size distribution in both accumulative pore volume and differential pore volume of baseline GDM compared to custom GDM is shown in **Figure 30.** Adding two different micro porous layers greatly reduces the volume of large pores.

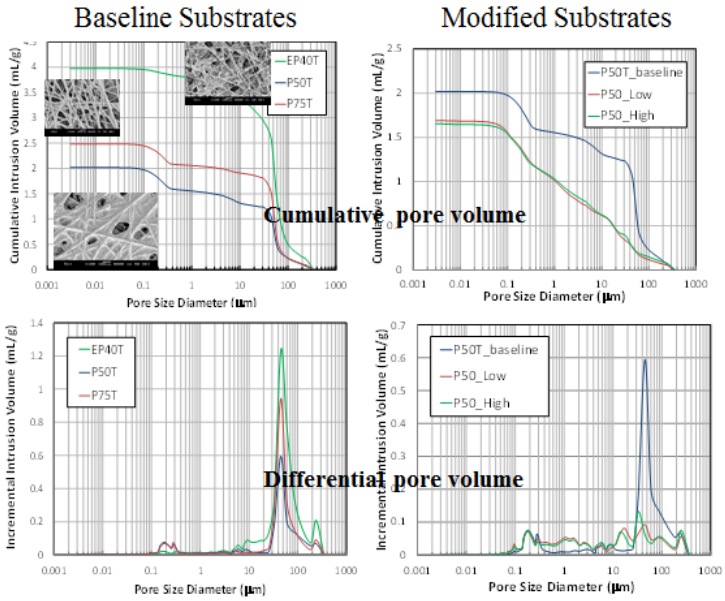

Figure 30. Comparison of mercury pore size distributions of new design GDM

The SEM images on the substrate surfaces and cross-section of custom GDL compared to baseline GDL are shown in **Figure 31**. Figure 31a shows EP40 GDM; Figure 31b shows P75 GDM.

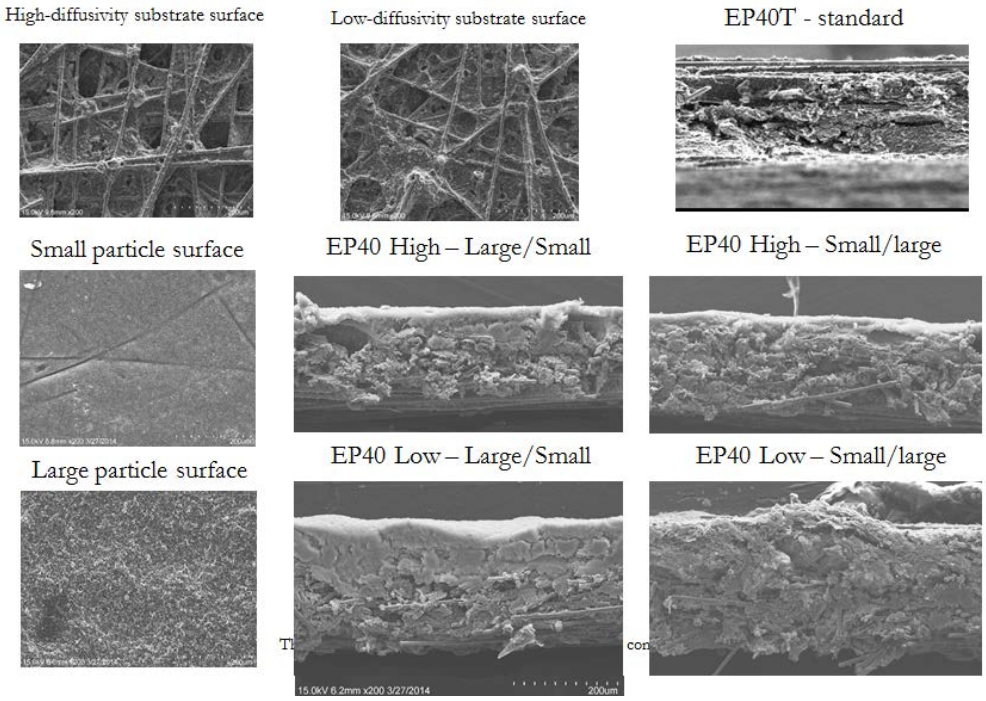

(a)

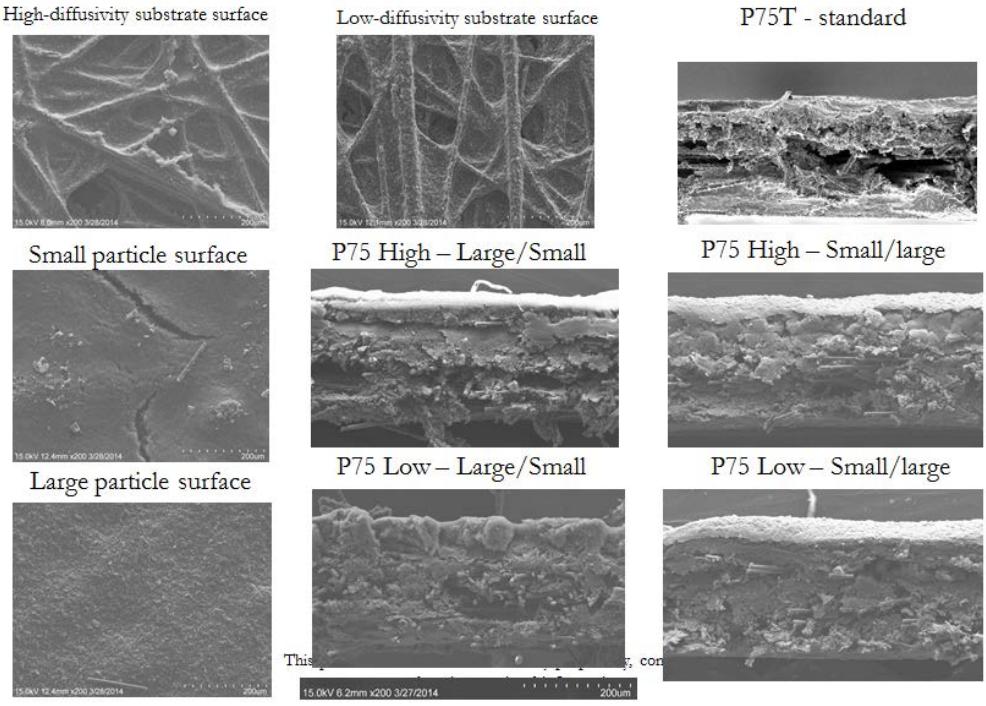

(b)

Figure 31. Structure of GDM: a) EP40 and b) P75

Table 4 lists the status of samples and experiments using twelve custom GDM compared with standard GDM. In this table the measurement of MacMullin number from those GDM is also provided. The inlet humidity conditions were set at 25%/25% RH, 75%/25%RH, and 100%/50%RH with 5 psi on anode/cathode. GORE ™ MEA57 series was used in each case.

Table 4. Custom GDM Compared with Commercial Standard

Substrate	Diffusivity	MPL1	MPL2	MacMullin No.	Status
P50T				3.09	Done
P50	Low	Large	Small	2.63	Done
P50	High	Large	Small	2.18	Done
P50	Low	Small	Large	4.04	Done
P50	High	Small	Large	2.73	Done
P75T				4.43	Done
P75	Low	Large	Small	2.14	Done
P75	High	Large	Small	1.92	Done
P75	Low	Small	Large	11.11	Done
P75	High	Small	Large	2.63	Done
EP40T				3.70	Done
EP40	Low	Large	Small	5.18	Done
EP40	High	Large	Small	2.34	Done
EP40	Low	Small	Large	3.18	Done
EP40	High	Small	Large	2.62	Done

The new design of GDLs have been modified from standard AvCarb GDLs by adding two micro porous layers. Each set has been treated with two different methods in order to provide two different values of diffusivity

The performance comparison and predictions of three main substrates are shown in **Figure 32** (i.e. P50, P75, and EP40, with large carbon particle in MP1 and small carbon particle in MP2.

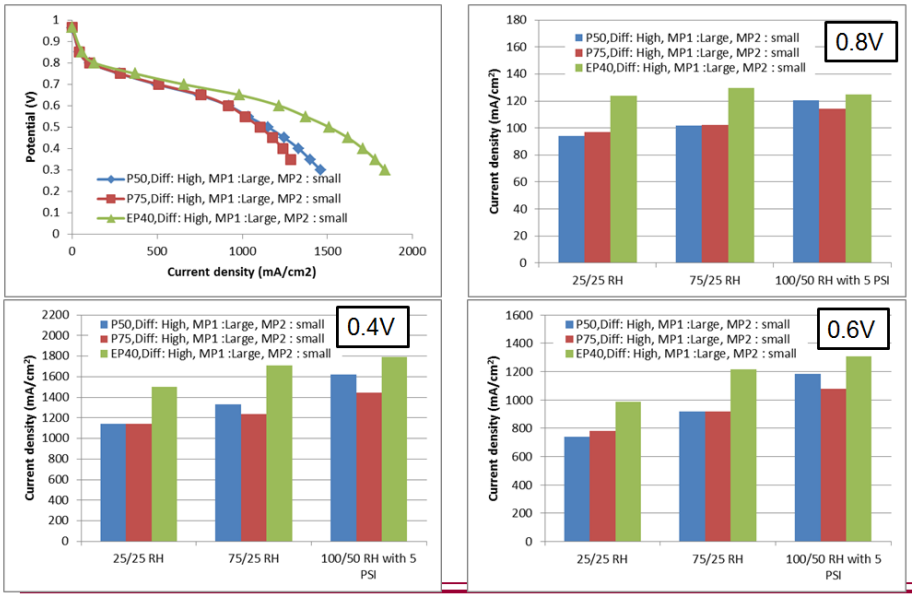

Figure 32. The performance comparison of different types of substrate, P50, P75, and EP40, under LARGE carbon particle of MP1 and SMALL carbon particle of MP2 with HIGH diffusivity. The cell temperature is 80°C with Stoich of 1.5/2.0 - Anode/cathode. The humidity conditions in the form of %RH are 25/25, 75/25 (VI curves are shown), and 100/50 with 5 psi.

These GDM were treated to increase the value of diffusivity to be greater than 0.25 cm^2/s or so-called high diffusivity. Furthermore, this figure consists of a summary of polarization curves at 75%/25% RH and three potentials with bar graph comparisons under different inlet relative humidity conditions. In this figure, EP40 shows the best performance compared with other types, especially at dryer humidity conditions. When inlet humidity increases, the performance of those three GDM are close to each other. GDM P50 and P75 show similar performance at low inlet humidity conditions, but P50 gives slightly higher performance than P75 at higher inlet humidity conditions.

The performance comparison and prediction of three main substrates (i.e. P50, P75, and EP40) with large carbon particles in MP1 and small carbon particle in MP2 is shown in **Figure 33**. But these GDM were treated to reduce the value of diffusivity to be less than 0.15 cm^2/s or so-called low diffusivity. For low diffusivity, P50 gives the best performance compared to other GDM. Moreover, the P50 GDM's, performance does not change significantly with the change of diffusivity. For P75 and EP40 GDM, their performance is decreased with decreasing of diffusivity, thus lower than P50 GDL performance. The GDL P75 still shows the lowest performance in this case as well as the case with high diffusivity.

The performance comparison and prediction of three main substrates (i.e. P50, P75, and EP40) with small carbon particle in MP1 and large carbon particle in MP2 are illustrated in **Figure 34.** These GDM were treated for high diffusivity similar to the case in Figure 33. The overall performance of these three GDM is very close together. GDL P50 has slightly lower performance than others, especially at higher current density.

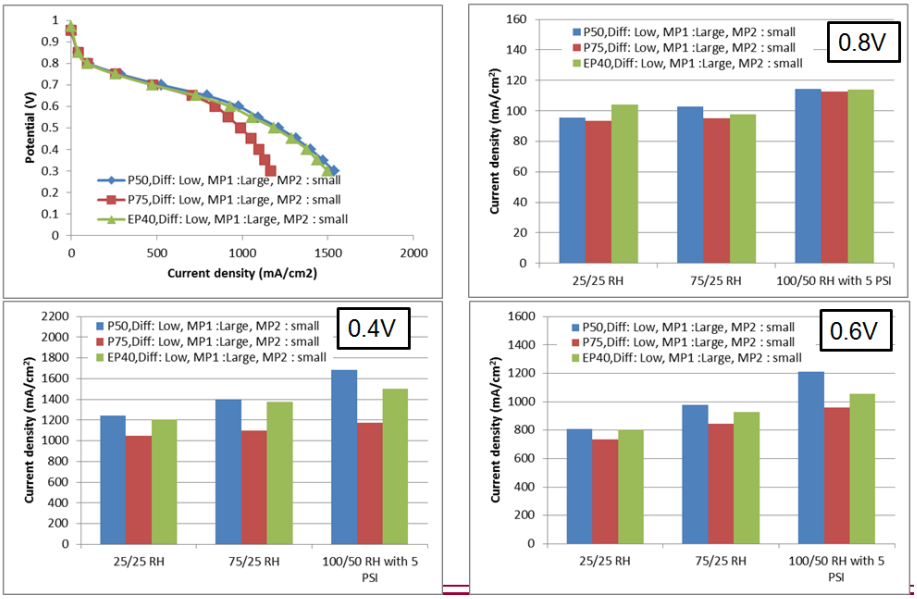

Figure 33. The performance comparison of different types of substrate, P50, P75, and EP40, under LARGE carbon particle of MP1 and SMALL carbon particle of MP2 with LOW diffusivity. The cell temperature is 80°C with Stoich of 1.5/2.0 - Anode/cathode. The humidity conditions in the form of %RH are 25/25, 75/25 (VI curves are shown), and 100/50 with 5 psi.

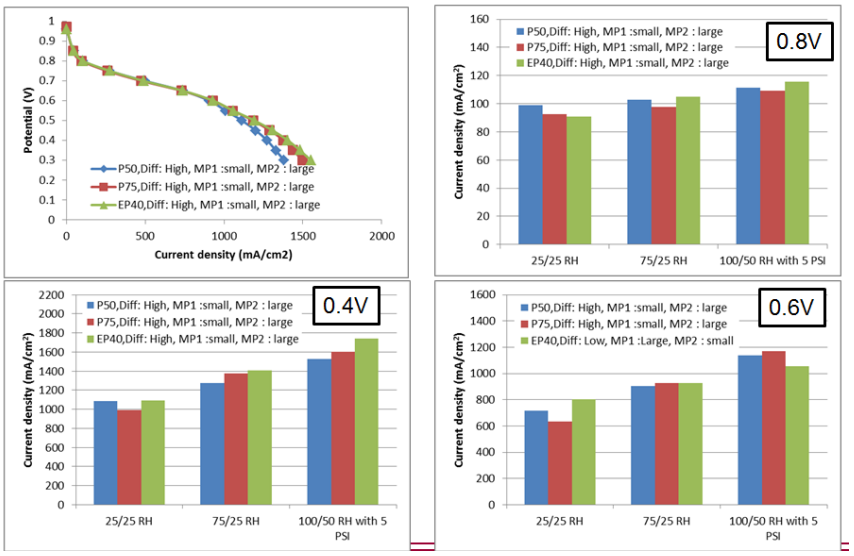

Figure 34. The performance comparison of different types of substrate, P50, P75, and EP40, under SMALL carbon particle of MP1 and LARGE carbon particle of MP2 with HIGH diffusivity. The cell temperature is 80°C with Stoich of 1.5/2.0 - Anode/cathode. The humidity conditions in the form of %RH are 25/25, 75/25 (VI curves are shown), and 100/50 with 5 psi.

Similar to Figure 34, **Figure 35** illustrates the performance comparison and prediction of three main substrates (i.e. P50, P75, and EP40) with small carbon particles in MP1 and large carbon particles in MP2. These GDM were treated for low diffusivity. For this treatment condition, GDL EP40 gives the highest performance for all operating conditions and GDL 75 shows the lowest performance. GDL P50 and P75 have much better performance when the small carbon particles face the membrane; however, for GDL EP40 the performance change is not significantly different from a single uniform particle size.

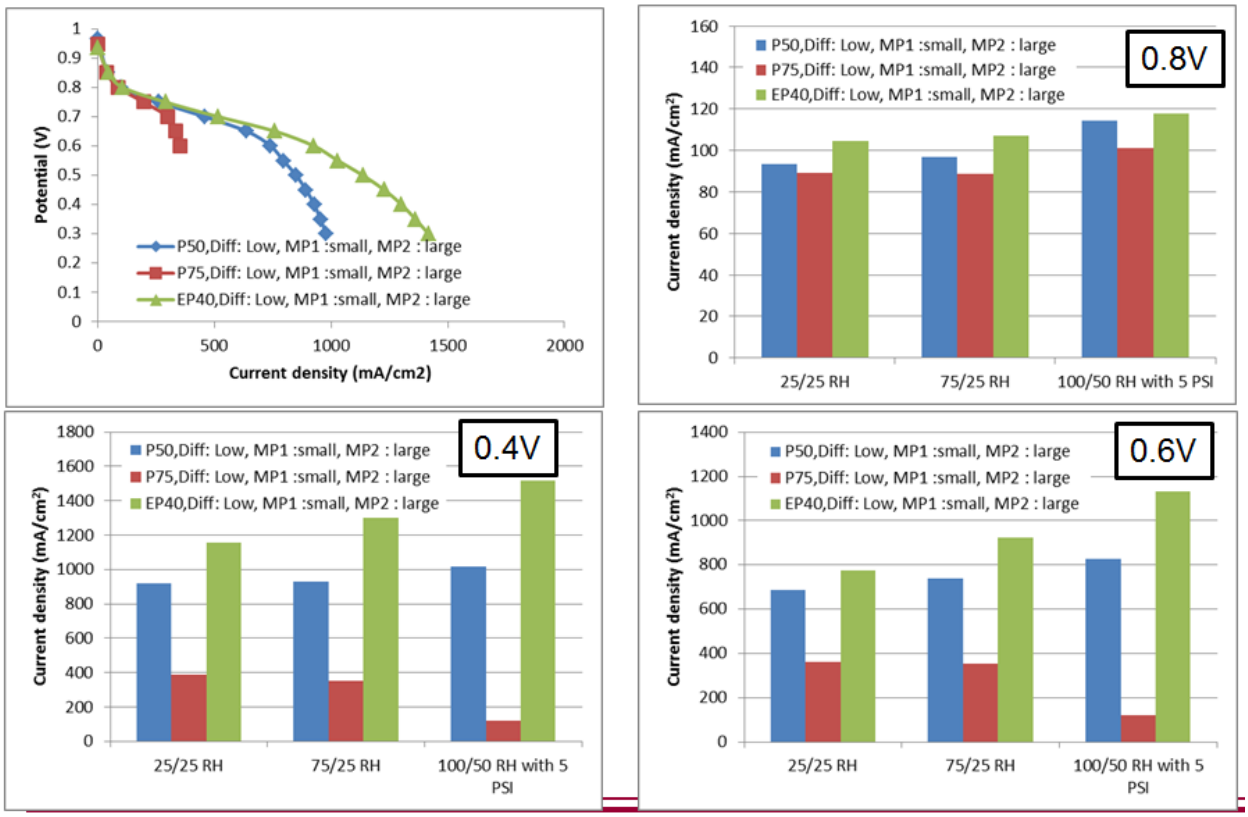

Figure 35. The performance comparison of different types of substrate, P50, P75, and EP40, under SMALL carbon particle of MP1 and LARGE carbon particle of MP2 with LOW diffusivity. The cell temperature is 80°C with Stoich of 1.5/2.0 - Anode/cathode. The humidity conditions in the form of %RH are 25/25, 75/25 (VI curves are shown), and 100/50 with 5 psi.

The current density distribution and membrane water content of custom GDM via CFD simulation are depicted in **Figure 36.** The simulation is under high diffusivity, MPL1-Large, and MPL2-Small at I_{avg} of 1 A/cm^2. P75 has the most non-uniform distribution and EP40 shows the most uniform distribution with high value of membrane water content. When the diffusivity of substrate is low, as shown in **Figure 37**, P75 also shows the most non-uniform distribution whereas EP40 gives the highest average value of membrane water content and also gives the most uniform distributions. From these two figures, when the diffusivity of substrate is reduced, the performance lowers and the uniformity of distributions worsens.

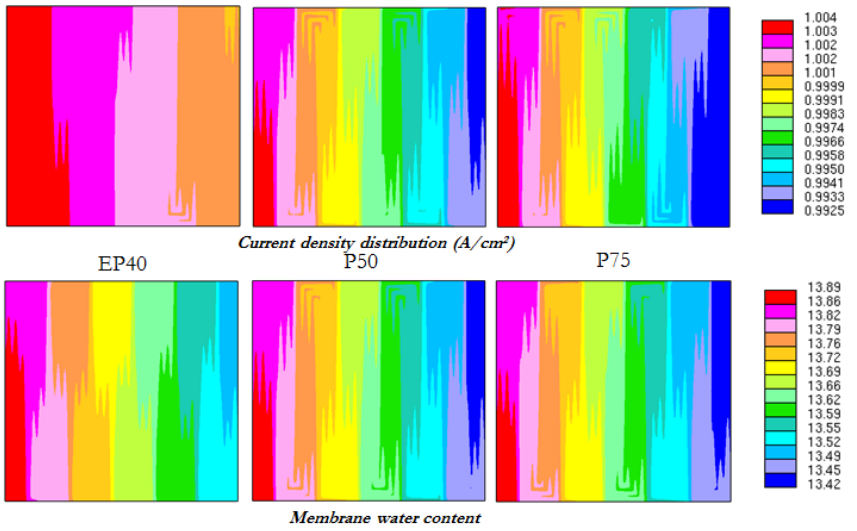

Figure 36. Current density distribution and membrane water content distribution of custom GDM under High-diffusivity, Large-MPL1, and Small-MPL2

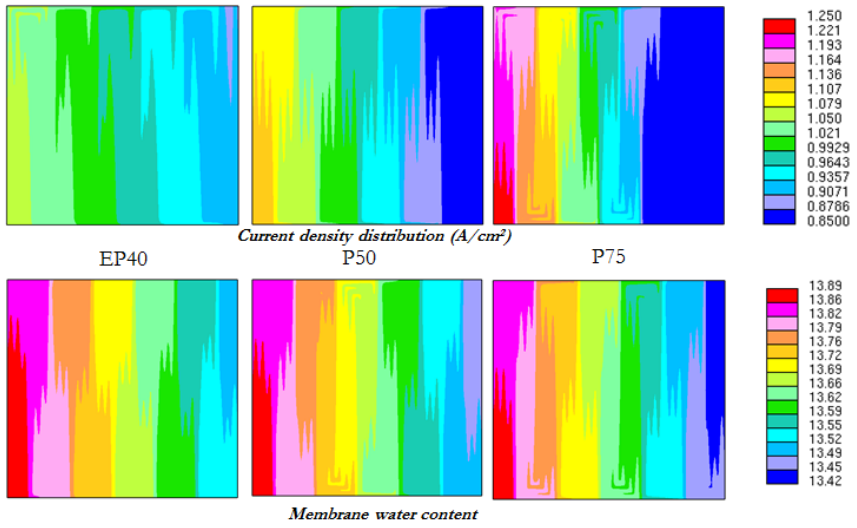

Figure 37. Current density distribution and membrane water content distribution of custom GDM under Low-diffusivity, Large-MPL1, and Small-MPL2

3.5 Flow Field Manufacturing

Tech-Etch manufactured flow fields per USC's specifications. The flow field design is shown in **Figure 38**: (a) Photo of actual flow fields; (b) Compression pressure pattern of parallel flow field at 30 in-lb. torque.

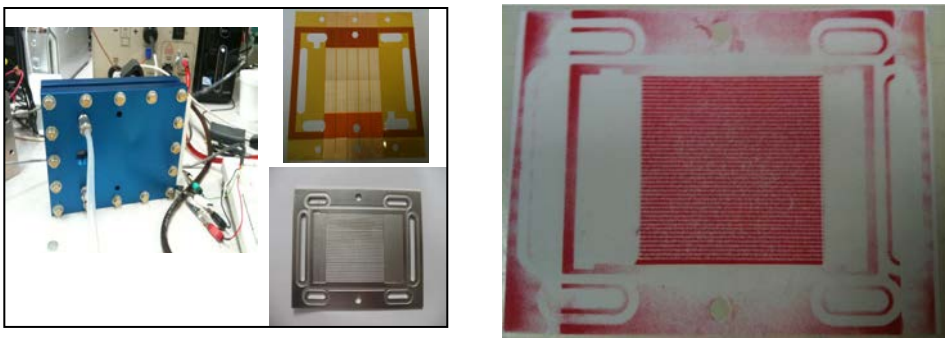

(a) Flow field (b) Pressure pattern

Figure 38. Flow field design

Giner obtained bipolar plate baseline flowpaths designed by General Motors and widely used for fuel cell testing for various membranes and diffusion media. Then USC completed model geometry for simulation and CAD drawing for the CBD for segmented-cell experiments. **Figure 39** shows GM plate assembly with (a) GM complete assembly fuel cell and (b) GM cell assembly with CBD.

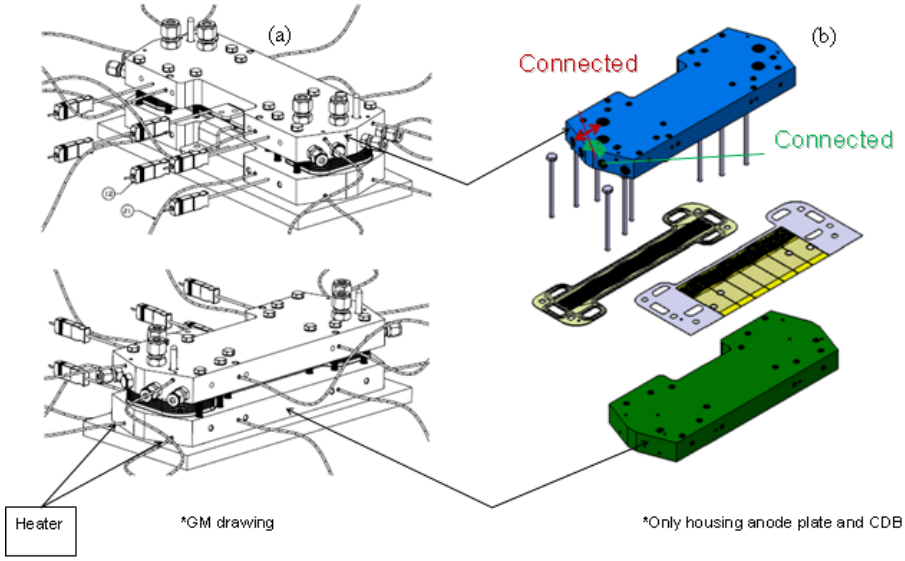

Figure 39. Assembly of GM bipolar plates with flow channels

3.6 New Membrane Performance

The fabrication of dimension-stabilized BPSH-6FPAEB membrane is shown in **Figure 40**. First, ionomer powder received from VA Tech was dissolved in N-methylpyrrolidone (NMP). The dissolved ionomer was then cast onto a thin Teflon® film substrate. The laser-machined Kapton film (6- to 8-µm-thick support structures with 8- to 20-µm-diameter holes and 50% porosity) was sandwiched between two Teflon substrates that were already deposited with the ionomer. The sandwiched components were subsequently subjected to hot press at appropriate pressure for

decal transfer. The ionomer films were peeled off from the two Teflon substrates as they were coated to two sides of the Kapton support.

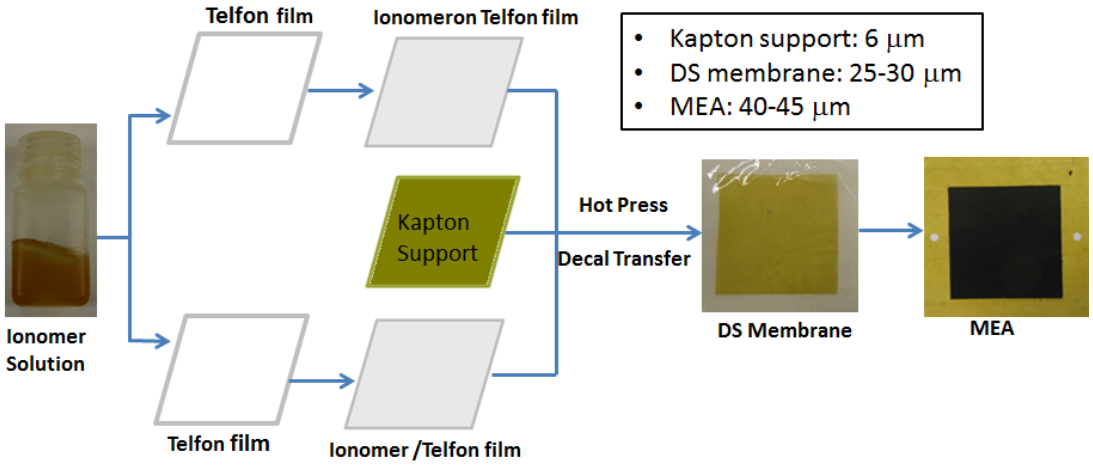

Figure 40. Fabrication of dimension-stabilized VA Tech membranes

In this period, the new lot of 25-cm^2 membranes provided by VA Tech were made into MEAs at Giner and tested at USC for performance, water balance measurement, and model validation under hydrogen and air. Four operating conditions were shown in this report, as shown in **Table 5.**

Table 5. Fuel Cell Operating Conditions

Case No	Anode Stoich	Anode RH (%)	Anode T (°C)	Anode back P (kPa)	Cathode Stoich	Cathode RH	Cathode T(°C)	Cathode back P (kPa)
1	1.5	75	80	101	2.0	25	80	101
2	1.5	50	80	101	2.0	50	80	101
3	1.5	100	80	101	2.0	50	80	101
4	1.5	95	80	101	2.0	95	80	101

The polarization curves of operating conditions shown in Table 5 is presented in **Figure 41**. In each figure there are polarization curves of experiment, experimental data of higher frequency resistance (HFR), polarization curve after IR correction, CFD prediction of polarization curve, and CFD prediction of HFR. The CFD prediction agrees well with experimental data for both polarization curve and HFR for all cases. From those figures, HFR decreases when the humidity is increased as expected for both experimental and numerical prediction. It is interesting to report that with this VT membrane, the membrane resistance is more controlled by anode humidity rather than by cathode humidity. Due to lower membrane water diffusivity of this VT membrane compared to Nafion as given in the last report, more electro-osmotic drag from anode to cathode is likely controlling water transport across the membrane.

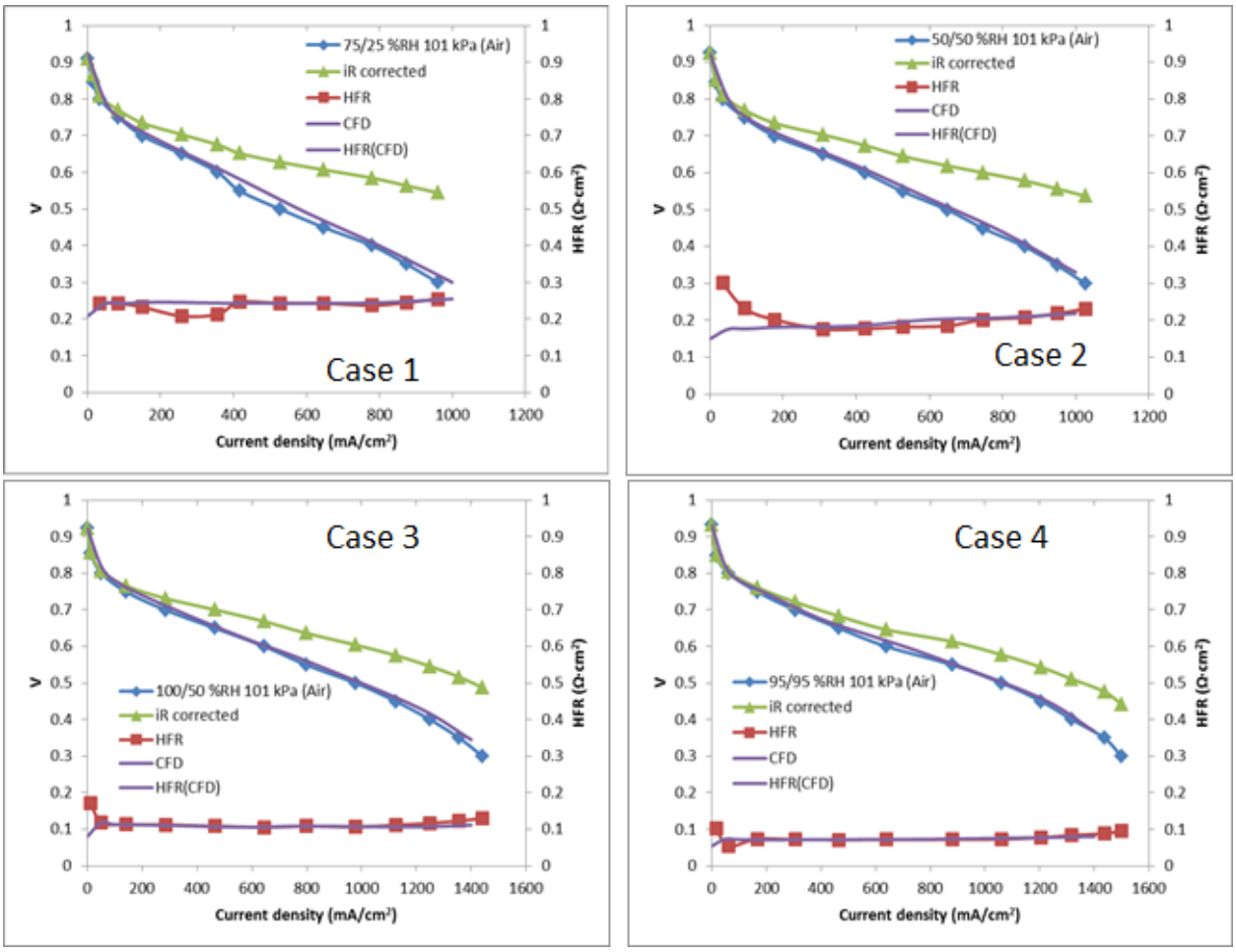

Figure 41. Performance of VA Tech BPSH-6FPAEB membrane at different operating conditions

The polarization curve comparison with different inlet humidity conditions using VT membrane is shown in **Figure 42**. From this figure, the humidity of Case 3 (100%/50% RH) and Case 4 (95%/95% RH) gave similar performance due to similar HFR as shown in Figure 41. For inlet humidity of Case 1 (75%/25% RH) and Case 2 (50%/50% RH), they also show similar performance, but lower than Cases 3 and 4.

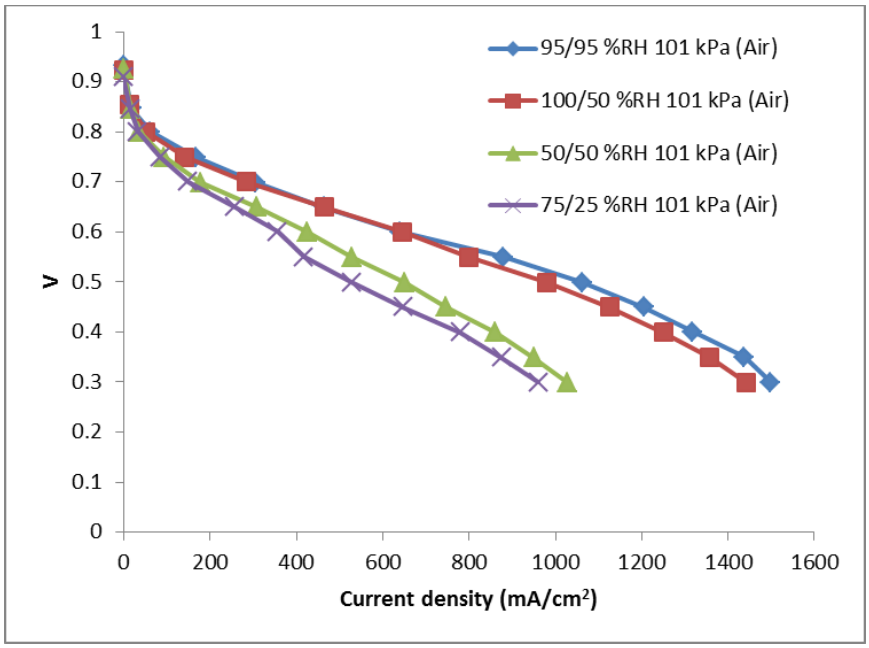

Figure 42. The effect of humidity on PEMFC performance using VT membrane

The water balance experiment and numerical prediction are shown in **Table 6**. In this table, three inlet humidity conditions (Cases 1, 2 and 4) and four current densities (0.4, 0.6, 0.8, and 1.2 A/cm^2) were chosen to compare and analyze. The procedure of water balance measurement was stated in a previous report and AMR presentation. In general, we measure water coming in and going out at both the anode and cathode of fuel cell hardware. At each current setting, the water generation can be calculated. The overall mass balance of each side can quantify water transport across the membrane. A positive value represents water transport from anode to cathode; a negative number, water transport from cathode to anode. From this table, the model predictions of water balance agree well with experimental measurement within 10 percent error. The net water transport across the membrane shows the direction from anode to cathode for all cases. At the same inlet humidity, when the current is increased, the rate of water transport across membrane from anode is also increased due to higher electro-osmotic drag coefficient, EODC ($n_d \times \frac{I}{F}$). At the same current with the same humidity of both anode and cathode, increasing humidity of both anode and cathode also increases the rate of water transport across the membrane. Moreover, increasing the gradient of humidity between anode and cathode (i.e., 50%/25% RH vs. 75%/25 RH anode/cathode) also increases the rate of water transport across the membrane from anode.

Table 6. Water Balance

	i A/cm²	RH	Anode Water Balance (mg/sec)			Cathode Water Balance (mg/sec)				error (%)
			Water in	Water out	Cross to Cathode	Water in	Gen.	Water out	Cross from Anode	
EXP	**0.4**	75/25	0.75	0.22	0.53	0.59	0.93	2.01	0.49	7.5
CFD	**0.4**	75/25	0.75	0.23	0.52	0.59	0.93	2.03	0.51	2.0
EXP	**0.6**	75/25	1.12	0.33	0.79	0.88	1.40	3.09	0.81	2.5
CFD	**0.6**	75/25	1.12	0.31	0.81	0.88	1.40	3.13	0.85	4.7
EXP	**0.4**	50/50	0.42	0.29	0.13	1.35	0.93	2.42	0.14	7.1
CFD	**0.4**	50/50	0.42	0.29	0.13	1.35	0.93	2.40	0.12	8.3
EXP	**0.8**	50/50	0.85	0.55	0.30	2.70	1.87	4.88	0.31	3.2
CFD	**0.8**	50/50	0.85	0.58	0.27	2.70	1.87	4.85	0.28	3.5
EXP	**0.4**	95/95	1.10	0.86	0.25	3.51	0.93	4.73	0.29	13.7
CFD	**0.4**	95/95	1.10	0.90	0.20	3.51	0.93	4.66	0.22	9.0
EXP	**0.8**	95/95	2.21	1.68	0.53	7.03	1.87	9.44	0.54	1.8
CFD	**0.8**	95/95	2.21	1.66	0.55	7.03	1.87	9.45	0.55	0.0
EXP	**1.2**	95/95	3.32	1.99	1.34	10.55	2.80	14.60	1.25	7.5
CFD	**1.2**	95/95	3.32	2.01	1.31	10.55	2.80	14.72	1.37	4.4

VA Tech membrane 6FPAEB-BPSH (Lot#93) was combined with CDB to measure local current on 50-cm² serpentine flow field. The experimental results were compared and validated with numerical predictions. Work focused on high-humidity toward oversaturation conditions, 100/125% RH and 100/150% RH, as liquid water affects the performance of the PEMFC. The validation between modeling results and experimental data will give an accuracy level of modeling code for further analysis of water transport in the PEMFC single cell and stack. Local polarization curves measured from CDB are shown in **Figure 43**.

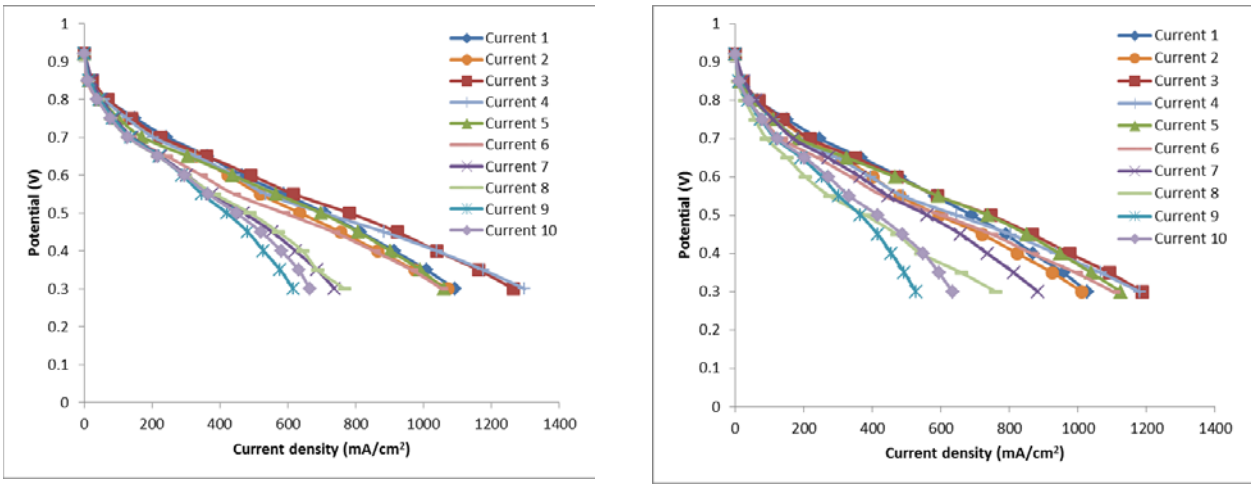

(a) 100/125%RH (b) 100/150%RH

Figure 43. Local polarization curves under different inlet humidity condition using VA Tech 6FPAEB-BPSH membrane

In the CDB, there are ten segments; therefore, ten polarization curves in a single cell can be reported. **Figure 43a** presents the curves for 100%RH on the anode and 125%RH on the cathode. **Figure 43b** shows the curves for 100%RH on the anode and 150%RH on the cathode. The numbers 1 to 10 represent the segments associated with flow direction. In this figure, both conditions reveal similar local performance profiles, but 100/125 %RH gives higher performance than 100/150 %RH.

To compare the experimental results with model predictions, the contour plot pattern was used. The experimental data of 10 segments were imported to plotting software for contour plot. **Figure 44** shows comparison of current density between experiment and model predictions for two inlet humidity conditions at a cell potential of 0.6 V. From this figure, the model predictions agree with experimental data for very high-humidity conditions. There is a significant drop in local performance at around the middle toward the exit of the cell observed in both experiment and modeling results, due to the high flooding in those areas. **Figure 45** presents the prediction of liquid water film thickness on the cathode membrane surface for both conditions. It shows that the thickness of liquid water is higher when inlet humidity of the cathode side is increased. As expected, the thicker the liquid water, the lower local performance shown in those areas. It also shows that with this oversaturated humidity condition on the cathode, the condensation of water vapor starts from the entrance event, though there is heat generated due to the high electrochemical reaction as shown in **Figure 46**.

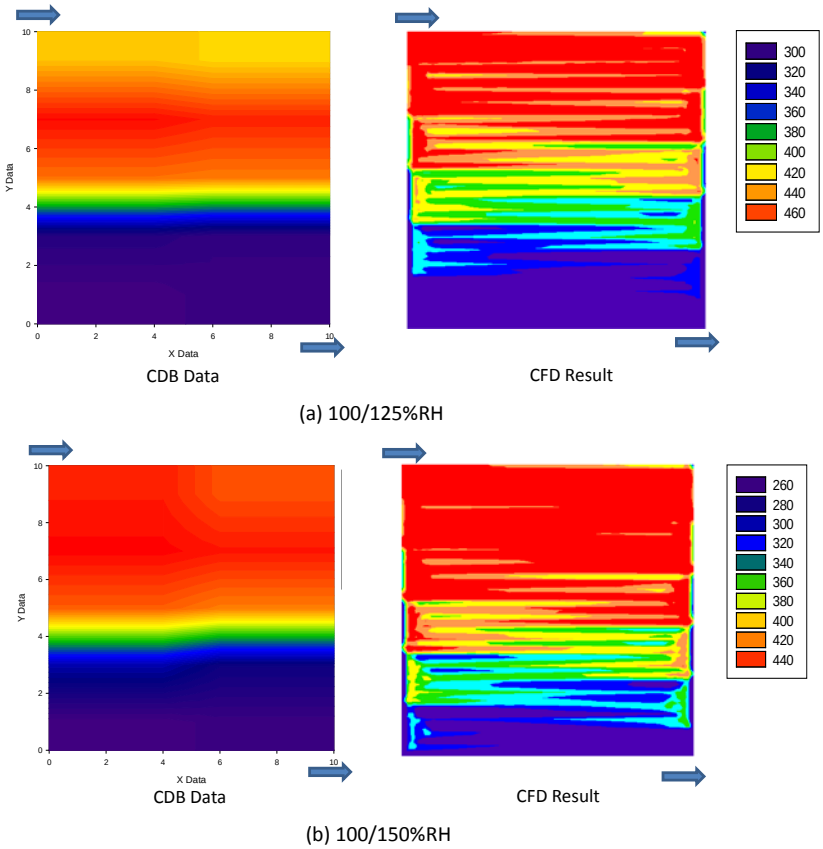

Figure 44. Current density distribution (mA/cm^2) under different inlet humidity condition, Experiment vs. Numerical Prediction at voltage of 0.6 V

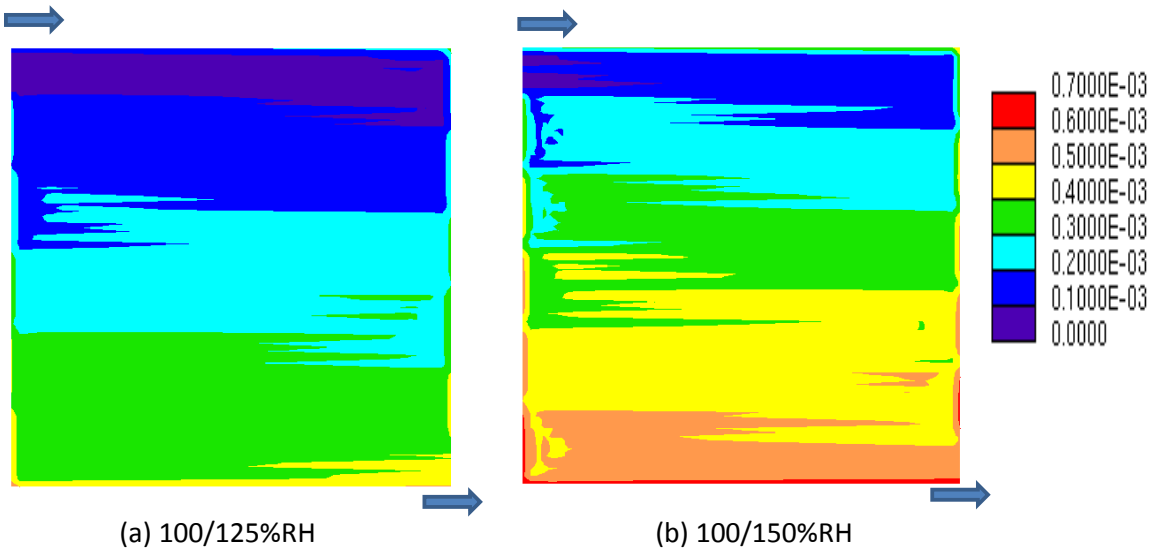

Figure 45. Prediction of liquid water film thickness (mm) on cathode membrane surface at different inlet humidity conditions for Vcell of 0.6 V

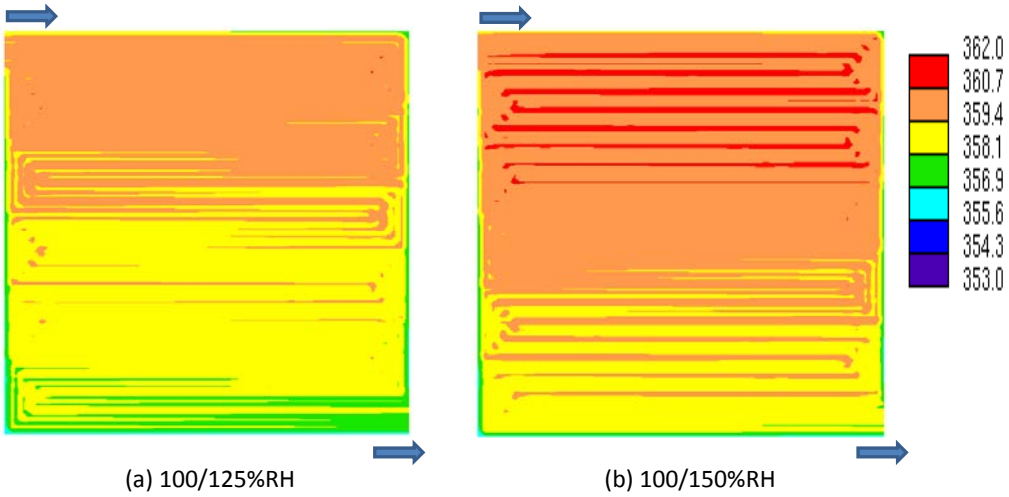

Figure 46. Prediction of temperature (K) on cathode membrane surface at different inlet humidity conditions for Vcell of 0.6 V

3.7 Modelling

To test the model PEM diffusivity, the model was altered to 6x and 1/6x that of PFSA membranes to investigate the effect of diffusivity on performance. Figure 46 shows simulated current density distribution on MEA surface at three water diffusivities and average current density of 0.6 A/cm^2 with (a) 75% /25% RH and (b) 25%/25% RH (anode/cathode). It is interesting that for both anode humidity conditions, the case of increasing diffusivity gives the most uniformity in current density distribution and 1/6Dw shows the most non-uniformity in distribution. Also, increasing diffusivity leads to the largest improvement in the dry anode case. This is not surprising as the water needs to diffuse to the anode to counter electro-osmotic drag.

The block copolymers being developed are expected to have a very different diffusivity than Nafion, and will be used to confirm these predictions.

The effect of EODC (n_d) on fuel cell performance and water uptake has been simulated. Standard equation of n_d for Nafion membranes is expressed below:

$$n_d(x,y,t) = 0.0029\lambda^2 + 0.05\lambda$$

Where, water uptake using an empirical equation shown below

$$\lambda = 0.043 + 17.81a_a - 39.85a_a^2 + 36.0a_a^3; 0 < a_a \le 1$$
$$= 14 + 1.4(a_a - 1); 1 < a_a \le 3$$

Here, a_a represents water activity or relative humidity. The equations for conductivity, (S/m), net water flux, α, and membrane diffusivity, D_w are expressed below:

$$\sigma_m(x,y,t) = \left(0.00514\frac{M_{m,dry}}{\rho_{m,dry}}C_{wa}(x,y,t) - 0.00326\right).\exp\left(1268\left(\frac{1}{303} - \frac{1}{T(x,y,t)}\right)\right)x10^2$$

$$\alpha(x,y,t) = n_d(x,y,t) - \frac{F}{I(x,y,t)}D_W(x,y,t)\frac{(C_{wc}(x,y,t) - C_{wa}(x,y,t))}{t_m}$$

$$D_W = D_\lambda \exp(2416(\frac{1}{303} - \frac{1}{T(x,y)});$$

where,

$D_\lambda = 10^{-10}, \lambda < 2;$

$D_\lambda = 10^{-10}(1 + 2(\lambda - 2)), 2 \le \lambda \le 3;$

$D_\lambda = 10^{-10}(3 - 1.67(\lambda - 3)), 3 < \lambda < 4.5;$

$D_\lambda = 1.25x10^{-10}, \lambda \ge 4.5$

The simulation is based on a small 2.56-cm^2 fuel cell at 80°C. Anode: 1.3 stoich, 100%, 75%, and 25% RH, 101kPa and cathode: 2.0 stoich, 25%RH, 101kPa.

Figure 47 shows the simulated effect of EODC (n_d) on PEMFC performance under different anode humidity. The decreased n_d (1/6 n_d) causes slight improvement of the cell performance at both RHs a) 100%/25% RH anode/cathode, and (b) 25%/25% RH anode/cathode. However, the increased (6 n_d) results in a significant drop of the cell performance. This is more pronounced at higher current densities and at lower RH. **Figure 48** even clearly illustrates the impact of anode humidity on the cell performance at three various EODCs while the cathode RH was fixed at 25%. Although lowering the EODC may lead to a performance increase, particularly at lower RH, this performance benefit is very small. Therefore, it might not be worthwhile making enormous efforts to develop new membranes with a reduced EODC. On the other hand, the increase of EODC is not a desired direction in membrane studies.

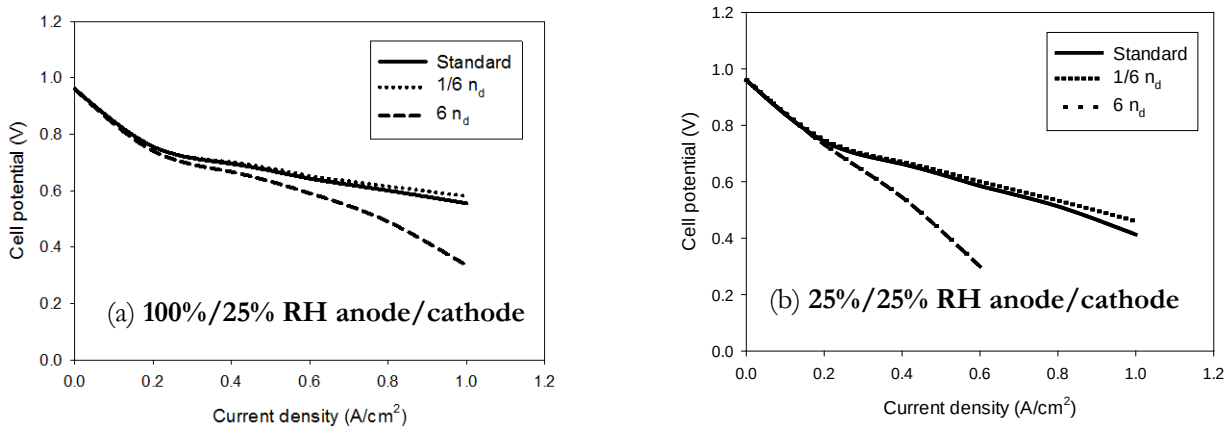

Figure 47. The effect of electro-osmotic drag coefficient (n_d) on fuel cell performance under different anode humidity

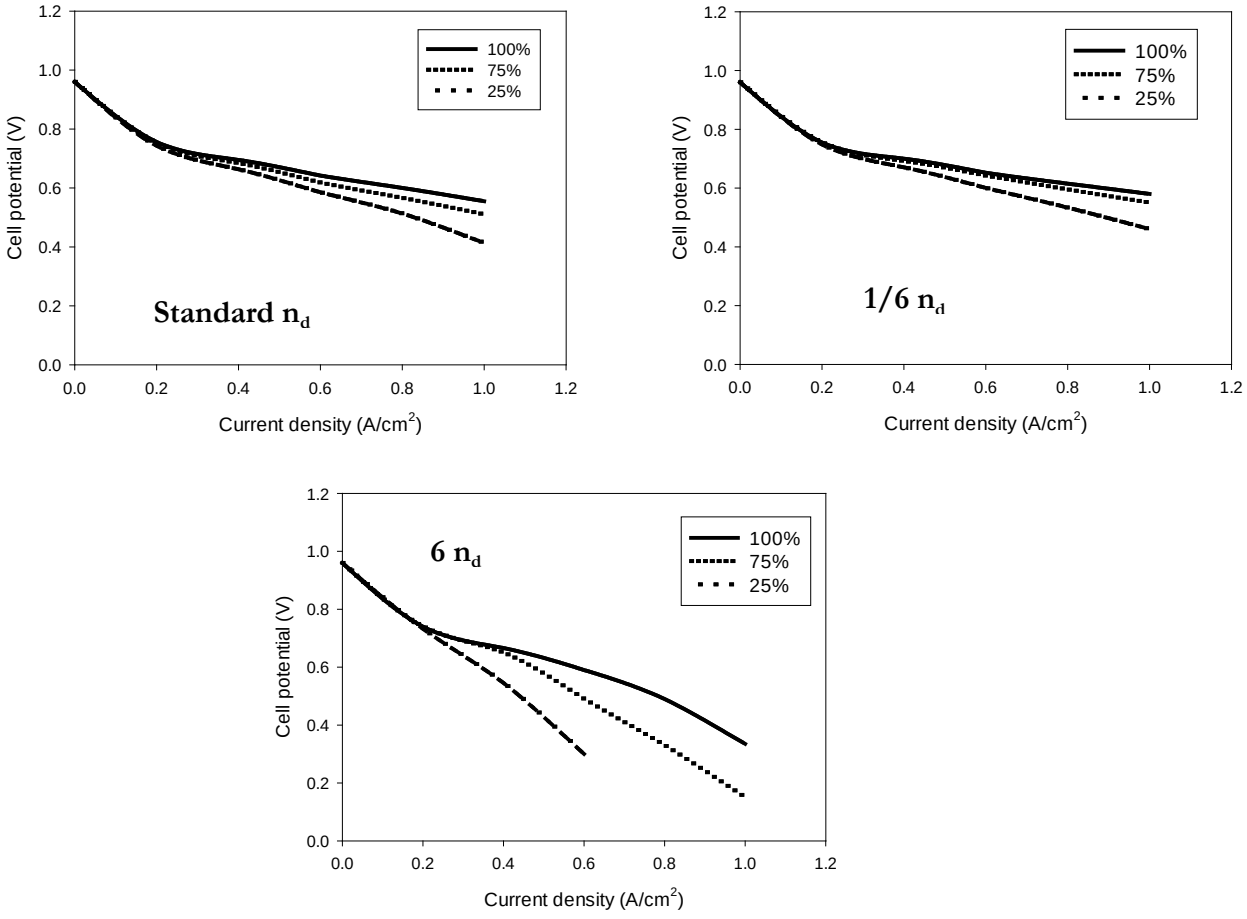

Figure 48. The effect of anode humidity on fuel cell performance under different electro-osmotic drag coefficient at fixed cathode humidity of 25%RH PEMFC performance under different anode humidity

The effect of EODC on fuel cell performance can be correlated to the membrane water uptake (λ). **Figure 49** shows the effect of EODC (n_d) on membrane water content under different anode humidity. It can be seen that the decreased EODC (1/6 n_d) improves the membrane water uptake for all the RHs. Significantly different is the increased EODC (6 n_d) that dramatically lowers the membrane water uptake. As the membrane loses water, its resistance increases and thus the fuel cell performance drops.

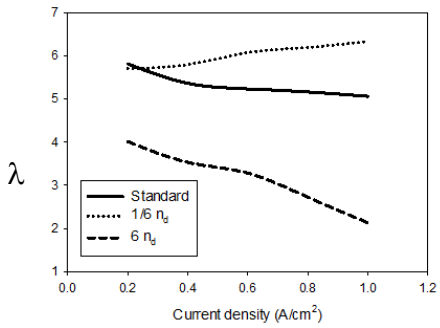

(a) **100%/25% RH anode/cathode**

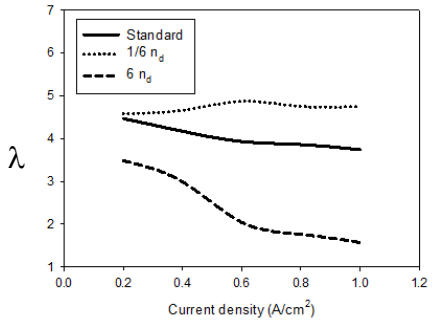

(a) **75%/25% RH anode/cathode**

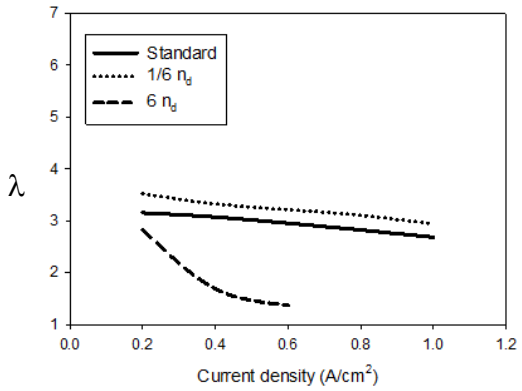

c) 25**%/25% RH anode/cathode**

Figure 49. Effect of electro-osmotic drag coefficient (n_d) on membrane water content

USC performed parallel flow-field modeling as shown in **Figure 50**. In the model, they used the empirical equations for the water uptake λ and EODC that were developed at Giner. The modeling is based on 2.5 million computational cells.

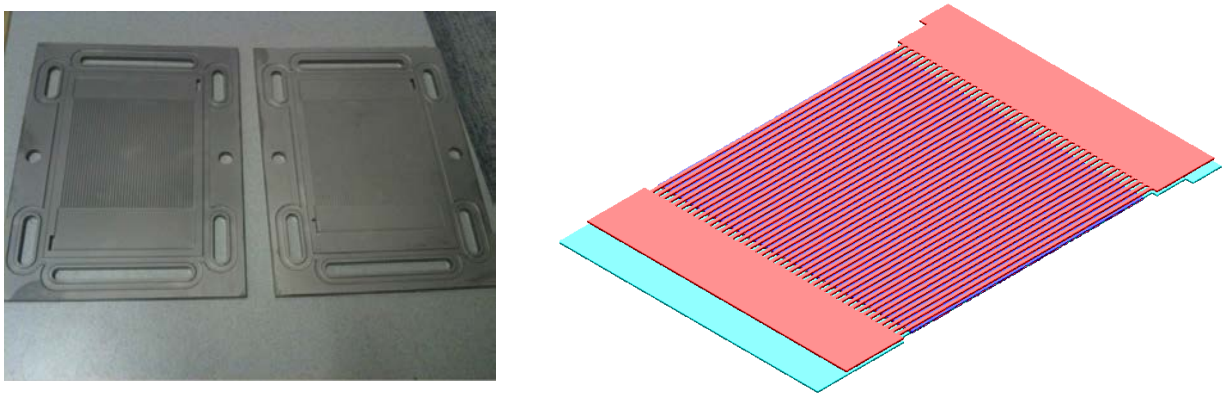

Figure 50. USC parallel flow field modeling

$$EODC = 0.2 + 9.5x10^{-2}\lambda + 2.9x10^{-3}\lambda^2 : 0 < \lambda < 5$$
$$EODC = 0.74 : \lambda \geq 5$$

The simulated current distribution along the flow field is shown in **Figure 51**. The condition was 75/25 %RH, 1.5/2.0 Stoich., 80°C, 101 kPa. The cathode inside also has the highest current while the current gradually drops from the cathode in to the cathode out. In the upcoming quarter we will operate the cell and compare to the simulated results.

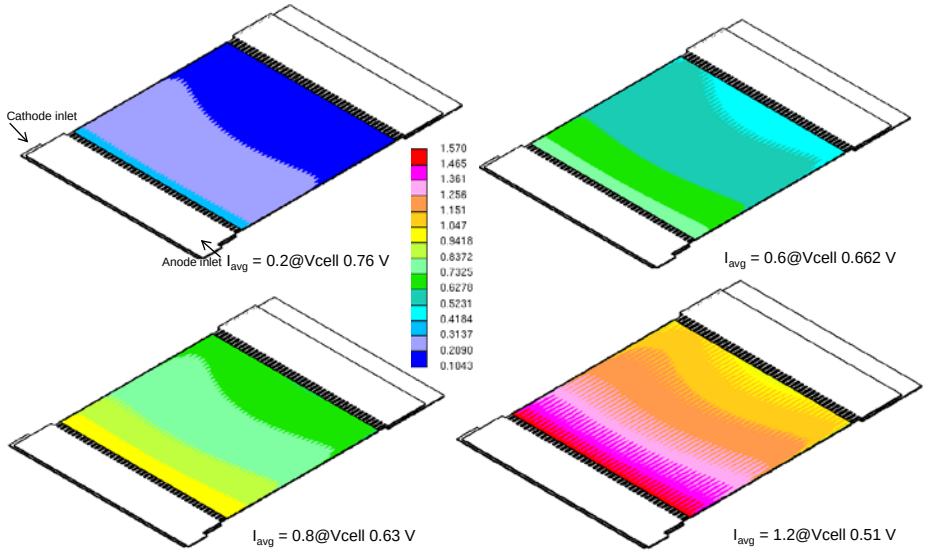

Figure 51. Simulated current distribution along parallel flow field

4.0 CHANGES IN APPROACH OR AIMS

Short stacks were never constructed or characterized as we used GM's open-source, short-stack 50-cm^2 hardware.

5.0 PROBLEMS

The project had an official start date of 11/1/2009, but we were not under contract until February 2010.

6.0 ABSENCE OR CHANGES IN KEY PERSONNEL

N/A

7.0 PRODUCTS PRODUCED OR TECHNOLOGY TRANSFER ACTIVITIES

Cortney Mittelsteadt *et al.*

- "Simultaneous Water Uptake, Diffusivity and Permeability Measurement of Perfluorinated Sulfonic Acid Polymer Electrolyte Membranes," *ECS Transactions*, **41**(1) 101-121 (2011)
- "Novel Current Distribution Board for PEM Devices," *ECS Transactions*, **41**(1) 549-559 (2011)
- "Transport in PEMFC Stacks," presented in *DOE Hydrogen and Fuel Cell Merit Review Meeting*, Arlington, VA, May 2011, 2012 and 2013
- "Novel System for Characterizing Electro-Osmotic Drag Coefficient of Proton Exchange Membranes," presented in *220th Meeting of ECS*, Abstract #1304, Honolulu, October 2012
- "Characterizing Water Transport Properties of Hydrocarbon Block Copolymer Proton Exchange Membranes," in *222nd Meeting of ECS*, Abstract #1344, San Francisco, October 2013

John Van Zee *et al.*

- M.J. Martinez-Rodriquez, C. Tong, S. Shimpalee, and J.W. Van Zee, "Characterization of Microporous Layers in Carbon Paper GDL for PEM Fuel Cell," in *ECS Transactions*, **33**(1), Polymer Electrolyte Fuel Cells 10, The Electrochemical Society, pp. 1133-1141 (2010).
- S. Shimpalee, V. Lilavivat, H. McCrabb, A. Lozano-Morales, J.W. Van Zee, "Understanding the effect of channel tolerances on performance of PEMFCs," *Intl. J. of Hydrogen Energy*, **36**(19), 12512-12523 (2011).
- M. Martinez, S. Shimpalee, T. Cui, B. Duong, S. Seraphin, J.W. Van Zee, "Effect of microporous layer on MacMullin number of carbon paper gas diffusion layer," *J. of Power Sources*, **207**(1), 91-100 (2012).

- "A novel current distribution board to understand local transport in PEMFCs ", presented in *220th Meeting of ECS*, Abstract #1545, Honolulu, October 2012
- V. Lilavivat, S. Shimpalee, H. Xu, J. W. Van Zee, and C. K. Mittelsteadt, "Novel current distribution board for PEMFC," submitted to *Intl J. of Hydrogen Energy* (2013).
- V. Lilavivat, S. Shimpalee, H McCrabb, and J. W. Van Zee, "Fundamental Analyses, Observations, and Predictions of Liquid Droplet Movement on Etched-Metal Surfaces for PEMFC," submitted to *Electrochimica Acta* (2013).

James McGrath *et al.*

- "Hydrophilic-Hydrophobic Multiblock Copolymer Electrolyte Membranes," *Progress in MEA 2010*, La Grande Motte, France, 19-22 September 2010.
- "Disulfonated Poly(Arylene Ether) Copolymers as Proton Exchange Membranes for H2/Air and DMFC Fuel Cells," *Advances in Materials for Proton Exchange Membrane Fuel Cell Systems 2011*, Asilomar Conference Grounds, Pacific Grove, CA. February 20 - 23, 2011.
- "Synthesis and characterization of multiblock partially fluorinated hydrophobic poly(arylene ether sulfone)-hydrophilic disulfonated poly(arylene ether sulfone) copolymers for proton exchange membranes," Chen, Yu; Rowlett, Jarrett R.; Lee, Chang Hyun; Lane, Ozma R.; Van Houten, Desmond J.; Zhang, Mingqiang; Moore, Robert B.; McGrath, James E. (2013) *Journal of Polymer Science, Part A: Polymer Chemistry*, published online: DOI: 10.1002/pola.26618.
- "Synthesis and characterization of multiblock semi-crystalline hydrophobic poly(ether ether ketone)-hydrophilic disulfonated poly(arylene ether sulfone) copolymers for proton exchange membranes," Chen, Yu; Lee, Chang Hyun; Rowlett, Jarrett R.; McGrath, James E., *Polymer*, **53**(15), 3143-3153 (2012).
- "Partly fluorinated poly(arylene ether ketone sulfone) hydrophilic-hydrophobic multiblock copolymers for fuel cell membranes", Chen, Yu; Guo, Ruilan; Lee, Chang Hyun; Lee, Myoungbae; McGrath, James E., *International Journal of Hydrogen Energy*, **37**(7), 6132-6139 (2012).
- "The effect of block length upon structure, physical properties, and transport within a series of sulfonated poly(arylene ether sulfone)s," Y. Fan, C.J. Cornelius, H.S. Lee, J.E. McGrath, M. Zhang, R.B. Moore and C.L. Staiger, *Journal of Membrane Science*, **430**, 106-112 (2013).
- Rowlett, J.R., Chen, Y., Shaver, A.T., Lane, O., Mittelsteadt, C., Xu, H., Zhang, McGrath, J.E., "Multiblock poly(arylene ether nitrile) disulfonated poly(arylene ether sulfone) copolymers for proton exchange membranes: Part 1 synthesis and characterization," *Polymer (United Kingdom)*, **54**(23) 6305 - 6313 (2013).

8.0 LIST OF SYMBOLS, ABBREVIATIONS, AND ACRONYMS

6FBPS0	hexafluoro biphenol sulfone
6FK	hexafluoro ketone
6FPAEB	hexafluoro bisphenol A benzonitrile
BPS100	biphenyl Sulfone
AFM	atomic force microscopy
BMP	Ballard Material Products, Inc.
CDB	current distribution board
CFD	computation fluid dynamics
DS	dimension stabilized
DSC	differential scanning calorimetry
EFT	Engineered Fibers Technology, LLC
EODC	electro-osmotic drag coefficient
GDL	gas-diffusion layer
GES	Giner Electrochemical Systems, LLC
Giner	Giner, Inc.
GM	General Motors
HQS100	hydroquinone sulfone
HFR	higher frequency resistance
MEA	membrane electrode assemblies
MPL	micro-porous layer
NMP	*N*-methylpyrrolidone
PEM	proton-exchange membrane
RH	relative humidity
SAXS	small angle X-ray scattering
SEM	scanning electron microscopy
SQSH	sulfonated quinone-**s**ulfone, H^+ form
TEM	transmission electron microscopy
USC	University of South Carolina
VA Tech	Virginia Polytechnic Institute and State University

9.0 BIBLIOGRAPHY & REFERENCES CITED

None.